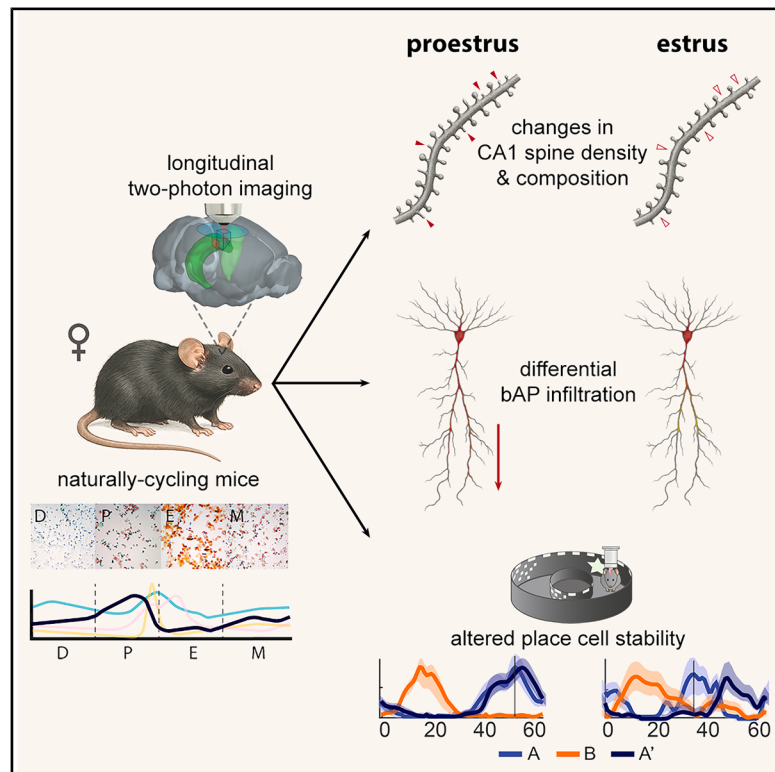


The estrous cycle modulates hippocampal spine dynamics, dendritic processing, and spatial coding

Graphical abstract



Authors

Nora S. Wolcott, William T. Redman,
Marie Karpinska, Emily G. Jacobs,
Michael J. Goard

Correspondence

michaelgoard@ucsb.edu

In brief

In this study, Wolcott et al. explore estrous-cycle modulation of hippocampal neuron structure and function. Using longitudinal two-photon imaging across the estrous cycle, they find significant modulation at the synaptic, cellular, and population levels.

Highlights

- In apical CA1 dendrites, spine density is robustly modulated by the estrous cycle
- A subset of the new spines appearing in proestrus become stable
- The degree of bAP spread into the apical dendrite depends on the estrous stage
- The estrous cycle modulates the stability of CA1 spatial representations

Article

The estrous cycle modulates hippocampal spine dynamics, dendritic processing, and spatial coding

Nora S. Wolcott,¹ William T. Redman,^{2,3} Marie Karpinska,^{4,5} Emily G. Jacobs,^{5,6,7} and Michael J. Goard^{1,5,7,8,*}

¹Department of Molecular, Cellular, and Developmental Biology, University of California, Santa Barbara, Santa Barbara, CA 93106, USA

²Interdepartmental Graduate Program in Dynamical Neuroscience, University of California, Santa Barbara, Santa Barbara, CA 93106, USA

³Intelligent Systems Center, Johns Hopkins University Applied Physics Laboratory, Laurel, MD 20723, USA

⁴Department of Computer Science, University of California, Santa Barbara, Santa Barbara, CA 93106, USA

⁵Department of Psychological & Brain Sciences, University of California, Santa Barbara, Santa Barbara, CA 93106, USA

⁶Ann S. Bowers Women's Brain Health Initiative, University of California, Santa Barbara, Santa Barbara, CA 93106, USA

⁷Neuroscience Research Institute, University of California, Santa Barbara, Santa Barbara, CA 93106, USA

⁸Lead contact

*Correspondence: michaelgoard@ucsb.edu

<https://doi.org/10.1016/j.neuron.2025.04.014>

SUMMARY

Histological evidence suggests that the estrous cycle exerts a powerful influence on CA1 neurons in the mammalian hippocampus. Decades have passed since this landmark observation, yet how the estrous cycle shapes dendritic spine dynamics and hippocampal spatial coding *in vivo* remains a mystery. Here, we used a custom hippocampal microperiscope and two-photon calcium imaging to track CA1 pyramidal neurons in female mice across multiple cycles. Estrous cycle stage had a potent effect on spine dynamics, with spine density peaking during proestrus when estradiol levels are highest. These morphological changes coincided with greater somatodendritic coupling and increased infiltration of back-propagating action potentials into the apical dendrite. Finally, tracking CA1 response properties during navigation revealed greater place field stability during proestrus, evident at both the single-cell and population levels. These findings demonstrate that the estrous cycle drives large-scale structural and functional plasticity in hippocampal neurons essential for learning and memory.

INTRODUCTION

Circulating sex steroid hormones exert a powerful, but poorly understood, impact on neuronal structure and function.^{1,2} In particular, receptors for the ovarian hormones 17 β -estradiol and progesterone are highly expressed in the hippocampus,^{2,3} a region critical for episodic and spatial memory formation. These hormones drive complex intracellular signaling cascades and, in humans, promote functional reorganization of brain networks across the reproductive cycle.^{1,7–9} However, how these endocrine signals shape neuronal processing and plasticity at the circuit level remains largely unknown.

Foundational *ex vivo* studies in the early 1990s revealed that dendritic spines—the primary site of excitatory synapses—undergo significant density fluctuations over the 4–5-day estrous cycle, particularly in apical CA1 dendrites.^{10–14} Subsequent work demonstrated that estradiol enhances excitatory synaptic plasticity by stimulating NMDA receptor insertion into the post-synaptic membrane of CA1 pyramidal neurons.¹⁵ The synaptogenic effects of endogenous estradiol have been observed in several mammalian species, including rodents and non-human primates.^{10,12,16} These effects are modulated by steroid hor-

mone receptors that engage both genomic and non-genomic pathways, resulting in widespread transcriptional, translational, and epigenetic changes.^{17,18} Moreover, recent human studies found that rhythmic steroid hormone fluctuations across the menstrual cycle coincide with structural changes in hippocampal subfields and widespread restructuring of functional connectivity.^{7,19,20} Together, these findings establish sex steroid hormones as potent neuromodulators of hippocampal circuits, yet we lack an understanding of how sex steroid hormones shape cellular and circuit-level processing *in vivo*.

Recent advances in multiphoton imaging techniques now allow for longitudinal tracking of dendritic processes across extended timescales,^{21–23} providing a powerful tool to bridge this knowledge gap. This allows us to address a range of outstanding questions: do spines that emerge in high-estradiol stages rapidly disappear, or are they stable across multiple cycles? How does spine turnover influence how CA1 neurons integrate excitatory input? Finally, how might these changes shape hippocampal responses and spatial coding?

Indirect evidence indicates that the estrous cycle may have profound effects on hippocampal function. For instance, new spines formed in response to estradiol administration form

functional synapses with new presynaptic partners.²⁴ This suggests that CA1 neurons likely experience increased excitatory synaptic input during high-estradiol stages, which may exert a powerful influence on cellular responses. This, in turn, could influence the activity of hippocampal place cells—a subset of CA1 neurons that encode spatial locations (place fields) within the animal's environment.^{4,25} The formation of place cells is dependent on local dendritic events,²⁶ so hormone-driven changes in dendritic excitability¹⁵ may alter place field stability, with broad implications for spatial memory and navigation.

Hippocampal place cells are highly adaptive, remapping their spatial representations in response to environmental changes such as visual cues, chamber shape, or reward location.^{27–29} When an animal returns to a familiar environment, place cells reinstate their original spatial maps.^{27,28} This flexibility is essential for allowing animals to successfully remember distinct environments.^{30–32}

Here, we used longitudinal two-photon imaging of naturally cycling female mice to determine the impact of the estrous cycle on CA1 neuron morphology and function. We found that dendritic spine dynamics, dendritic processing, and place cell stability all undergo pronounced estrous-dependent modulation. Together, these findings provide key insight into how endocrine fluctuations shape hippocampal circuits critical for spatial cognition, from the synapse to the circuit level.

RESULTS

The estrous cycle modulates dendritic spine turnover and morphology

The rodent estrous cycle spans 4–5 days and is divided into four stages: diestrus, proestrus, estrus, and metestrus.^{33–35} This cycle mirrors the hormonal fluctuations of the human 28-day menstrual cycle, in which estradiol levels rise through the follicular phase, peaking prior to ovulation (corresponding to the diestrus and proestrus stages), then drop sharply at the onset of the luteal phase (corresponding to the estrus stage; *Figure 1A*).^{7,34}

To determine estrous stage non-invasively, we used vaginal cytology, in which epithelial cells are collected via saline lavage and classified based on the relative proportion of cornified epithelial cells, nucleated epithelial cells, and leukocytes.^{34,35} However, this method is inherently subjective and has been shown to suffer from inter-examiner variability.^{36,38} To improve accuracy, we employed EstrousNet, a deep learning-based classifier that automates estrous stage identification (*Figure 1A*).³⁶ Classifications were performed post hoc and independently of the two-photon imaging to ensure that experimenters remained blind to the estrous stage.

Early cross-sectional work revealed significant estrous-modulated fluctuations in dendritic spine density on the apical dendrites of CA1 pyramidal neurons.^{10–14} These *ex vivo* studies demonstrated substantial hormonal modulation of synaptic density but lacked the ability to track individual spines across the estrous cycle. *In vivo* two-photon imaging enables such longitudinal tracking. However, hippocampal imaging typically requires neocortical aspiration and window implantation over CA1,³⁹ limiting optical access to CA1 apical dendrites, which extend ventrally from the soma.⁴⁰ To overcome this, we used chronically

implanted glass microperiscopes,³⁷ which allow optical access to CA1 apical dendrites, the primary site of estrous-driven synaptic remodeling (*Figure 1B*).¹⁰ To image dendritic spine morphology while minimizing background contamination, we used Thy1-GFP-M mice,⁴¹ which express GFP in a sparse subset of pyramidal neurons in the cortex and hippocampus (*Figures 1A* and *1B*).^{21–23,37,42–44} To resolve individual spines along the dendrite, we acquired images across multiple axial planes and generated composite projections via weighted averaging (*Figure 1C*). Noise was minimized using filtering and binarization, and single dendrites were segmented for longitudinal tracking (*Figure 1D*). Spine detection was automated with custom software and manually validated using an interactive graphical user interface (*Figure S1*; see **STAR Methods**).

Dendritic spines are classified into four primary morphological subtypes: filopodium, thin, stubby, and mushroom spines.^{45–47} We classified spines via a decision tree based on morphological parameters (*Figures 1E* and *S2*)⁴⁶ and evaluated density and turnover across estrous stages. Consistent with prior histological results, we found that spines were primarily added during the high-estradiol stage (proestrus) and pruned during the low-estradiol stage (estrus; *Figures 1E* and *1F*).

Across a sample of 21 dendritic segments from 6 mice, spine density fluctuated significantly as a function of estrous stage, analyzed using linear mixed effect models (LME) with fixed effect for estrous stage and random effects for mouse. During proestrus, spine density increased by $11.5\% \pm 0.2\%$ (mean \pm SEM) relative to the mean across stages ($p < 10^{-4}$, $F(1) = 36.98$, LME), while in estrus spine density decreased by $12.4\% \pm 0.2\%$ ($p < 10^{-4}$, $F(1) = 16.95$, LME; *Figure 1F*; *Table S1A*). Spine density during diestrus and metestrus was not significantly different from the global mean (D: $p = 0.1284$, $F(1) = 0.09$, M: $p = 0.6450$, $F(1) = 0.05$, LME; *Figure 1F*; *Table S1A*). These effects were consistent across dendrites and between mice (*Figures S3A* and *S3B*) and were not significantly modulated by the distance of spines from the soma (*Figures S3C–S3E*; *Table S1B*).

The estrous cycle differentially affected spine subtypes. Both thin spines ($p = 0.0026$, $F(3) = 5.16$, LME) and stubby spines ($p = 0.0025$, $F(3) = 5.19$, LME) showed significant modulation. By contrast, mushroom spine density remained stable across estrous stages ($p = 0.3277$, $F(3) = 1.17$, LME). Filopodia, which accounted for only 3% of total spines, were also not significantly modulated by estrous stage ($p = 0.1697$, $F(3) = 1.72$, LME; *Figure 1G*; *Table S1A*). However, the width of a typical filopodia falls below the functional diffraction limit of our imaging system and as a result may have been undercounted. Nonetheless, recent results indicate that filopodia are primarily silent synapses that do not contribute to excitatory neurotransmission.⁴⁸ Together, these findings reveal that the estrous cycle drives robust, estrous stage-dependent fluctuations in dendritic spine density, primarily affecting thin and stubby spines, which are likely to contribute to functional excitatory input and neuronal processing.⁴⁸

Morphological spine dynamics are shaped by estrous cycle stage

Longitudinal monitoring of dendritic morphology allows for detailed investigation of spine dynamics across the estrous

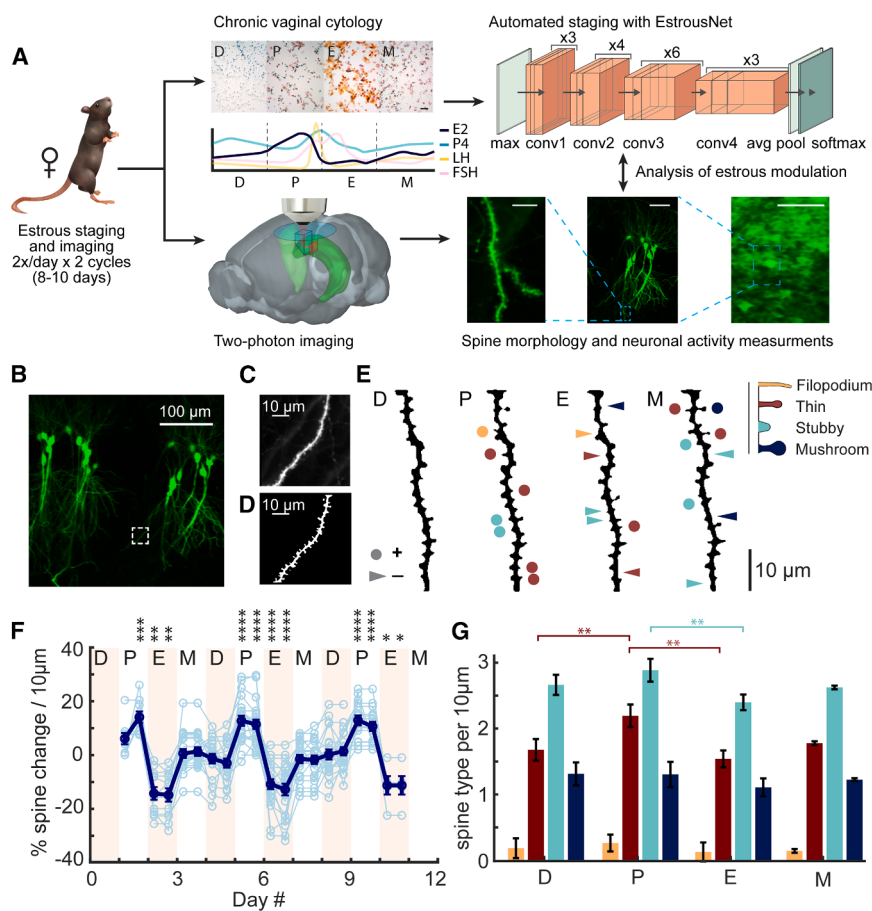


Figure 1. Dendritic spine density is longitudinally modulated by estrous-cycle stage

(A) Experimental pipeline. Left: measurements were taken from female mice every 12 h across two consecutive estrous cycles (8–10 days). Top center: vaginal lavage samples were collected and stained using Shorr stain, with images labeled by estrous stage (D, diestrus; P, proestrus; E, estrus; M, metestrus; scale bar, 1 mm). Relative ovarian hormone levels across stages are shown schematically for 17 β -estradiol (E2, navy), progesterone (P4, blue), luteinizing hormone (LH, yellow), and follicle-stimulating hormone (FSH, pink).³⁴ Top right: estrous stage classifications were performed using EstrousNet, a deep-learning model based on ResNet50 architecture.³⁶ Bottom center: two-photon imaging was used to track the structure or functional responses of hippocampal neurons across estrous stages using an implanted microperiscope.³⁷ Bottom right: representative frames from structural imaging of dendritic spines (scale bar, 10 μ m) and functional imaging of dendritic arbors (scale bar, 50 μ m) and CA1 populations (scale bar, 100 μ m). Imaging results are matched with estrous stage post hoc to analyze changes in neuronal structure and function.

(B) Example average projection of a transverse imaging plane of CA1 using a microperiscope in a Thy1-GFP-M mouse with sparse labeling of excitatory neurons.

(C) Weighted projection of the apical dendrite within the dashed box in (B).

(D) Filtered and binarized image of the dendrite in (C), used to detect and classify individual dendritic spines while masking extraneous processes.

(E) Dendritic spine dynamics across estrous stages. Binarized thresholded projections of a proestrus (P), estrus (E), and metestrus (M) dendrite. Circles indicate spine additions, triangles indicate spine subtractions, relative to the previous estrous stage. Color indicates spine type (yellow, filopodium; red, thin; blue, stubby; navy, mushroom).

(F) Spine density fluctuation across estrous stages. Percent change in spine density relative to baseline, recorded at 12-h intervals (D, diestrus; P, proestrus; E, estrus; M, metestrus); stage lengths were interpolated to 12-h bins for plotting consistency (see STAR Methods). Blue lines indicate spine densities for individual dendritic segments, and the bold navy line shows the average spine density (mean \pm SEM). Linear mixed effect model (LME) against the grand mean for all time points (* p < 0.1, ** p < 0.01, *** p < 0.001, **** p < 0.0001).

(G) Spine subtype distribution across estrous stages. Number of spines per 10 μ m dendritic segment as a function of estrous stage (mean \pm SEM; yellow, filopodium; red, thin; blue, stubby; navy, mushroom; D, diestrus; P, proestrus; E, estrus; M, metestrus; pairwise LME, Bonferroni-corrected; * p < 0.1, ** p < 0.01).

cycle. For instance, are new spines added during proestrus immediately pruned during estrus, or do they become a stable part of the synaptic population? To address this, we first measured the survival fraction of all dendritic spines as a function of time from the first session.^{49,50} After 10 consecutive recordings (5 days), $82.2\% \pm 2.2\%$ (mean \pm SEM) of spines present in the first session remained (Figure 2A), consistent with prior measurements in mixed-sex cohorts.³⁷ We then analyzed the stability of spines that appeared during proestrus, selecting only those that were absent during the previous diestrus stage and that were measured for a full cycle after their appearance. Upon entering estrus, $52.7\% \pm 5.7\%$ of these spines were rapidly pruned, yet $35.9\% \pm 3.2\%$ of proestrus-added spines remained after 10 sessions (Figure 2A). This indicates that while most spines added during proestrus are lost during estrus, a substantial fraction persist and are incorporated into the functional synaptic population.

To further examine the stability of proestrus-added spines, we categorized them as either transient (pruned at a point before completion of the subsequent cycle) or stable (maintained throughout the subsequent cycle). Compared with the general spine population (3% filopodium, 31% thin, 45% stubby, and 21% mushroom), transient spines had more (+13.4%) thin and (+5.8%) filopodia spines and fewer (-14.2%) mushroom spines (9% filopodium, 44% thin, 40% stubby, and 7% mushroom; Figures 2B and 2C). By contrast, stable spines had more (+9.0%) stubby spines and fewer (-6.2%) mushroom spines (0% filopodium, 31% thin, 54% stubby, 15% mushroom) than the general population (Figures 2B and 2D). Notably, thin spines were 13.1% less frequent in stable spines compared with transient spines, while stubby spines were 13.9% more frequent, suggesting that thin spines are more prone to pruning than their stubby counterparts (Figures 2C and 2D).

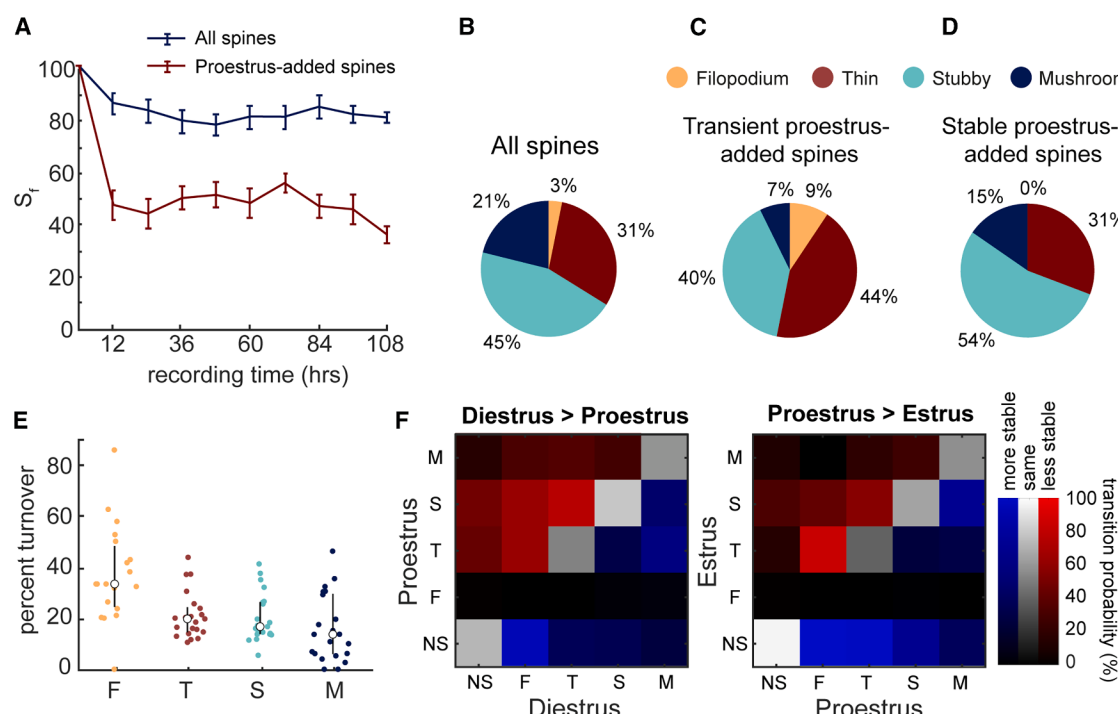


Figure 2. Dendritic spine properties dynamically shift across the estrous cycle

(A) Fraction of spines that remained present as a function of time since the initial observation (mean \pm SEM); red: all spines present on the first recording session; navy: spines that appeared during proestrus, where 0 h is the last session before estrus.

(B) The proportion of spine subtypes across the entire population of dendritic spines (yellow, filopodium; red, thin; blue, stubby; navy, mushroom).

(C) The proportion of spine subtypes for spines that appeared during proestrus but were immediately pruned during estrus (transient spines).

(D) The proportion of spine subtypes for spines that appeared during proestrus and were maintained throughout the subsequent cycle (stable spines).

(E) Percent turnover by session of all spines, analyzed respective to spine subtype (yellow, filopodium; red, thin; blue, stubby; navy, mushroom). Overlay indicates mean \pm SEM.

(F) Transition matrix for spine subtypes measured from diestrus to proestrus ($D > P$) and from proestrus to estrus ($P > E$), and spine subtypes are ordered from least to most stable (NS, no spine; F, filopodium; T, thin; S, stubby; and M, mushroom). Matrix elements are pseudocolored to indicate transitions to more stable subtypes (red), transitions to less stable subtypes (blue), and persistence of the same subtype (grayscale). Transition probability is shown by brightness, from 0% (black) to 100% (bright).

To quantify how spine stability varies by subtype, we analyzed the percent turnover per session and found a range of stability, ranked from least to most stable: filopodia ($32.3\% \pm 11.1\%$, mean \pm SEM), thin ($19.4\% \pm 5.0\%$), stubby ($16.7\% \pm 3.0\%$), and mushroom spines ($13.7\% \pm 7.8\%$; Figure 2E). Transition matrices revealed that spines preferentially transition from less stable to more stable subtypes during the transition from diestrus to proestrus (Figure 2F, left). Conversely, from proestrus to estrus spines are more likely to be pruned entirely rather than transitioning to less stable spine subtypes (Figure 2F, right). The subset of stable proestrus-added spines demonstrated a gradual increase in length, width, and brightness across the subsequent cycle (Figure S2E). These findings suggest that, in addition to spinogenesis and spine pruning, estrous-driven morphological changes may alter functional connectivity within the hippocampal circuit.

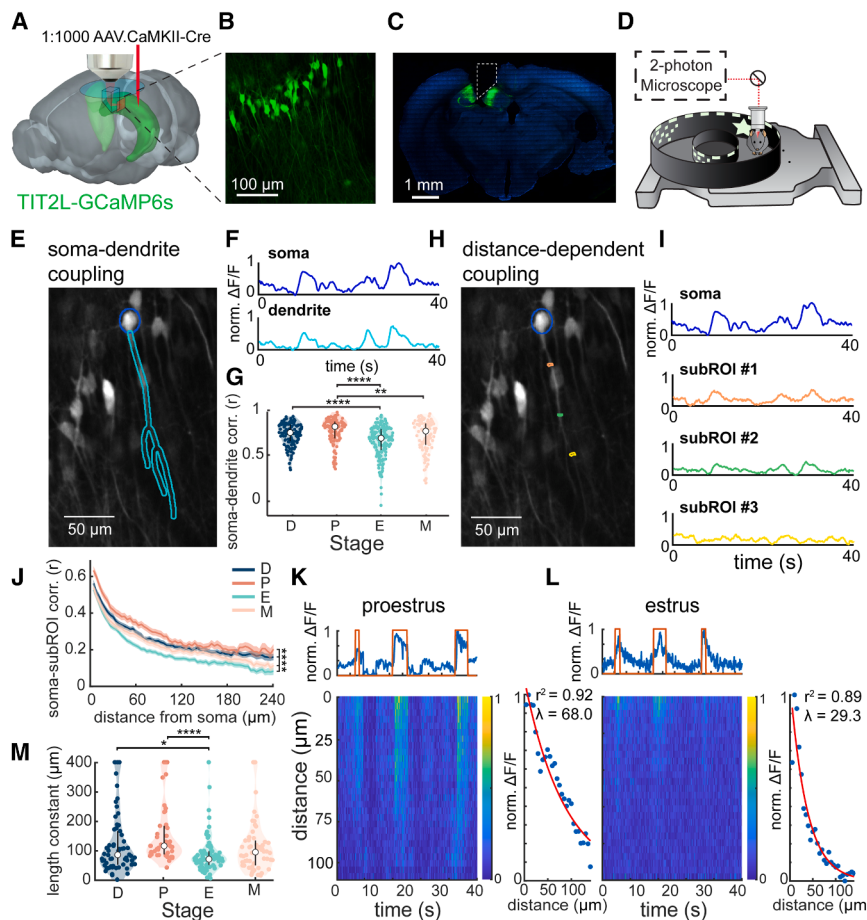
Somatodendritic coupling fluctuates across the estrous cycle

Given the significant changes in spine turnover observed across estrous stages (Figure 1F), we next investigated whether den-

dritic activity in CA1 was similarly estrous-modulated. To this end, we used a transgenic mouse line with Cre-dependent expression of GCaMP6s—a genetically encoded calcium indicator⁵¹—injected with diluted CaMKIIα-Cre virus. This achieved sparse and stable GCaMP6s expression in CA1 pyramidal neurons while minimizing neuropil contamination (Figures 3A and 3B; Video S1). To target apical dendrites, the primary site of estrous-mediated spine turnover,^{10–13} we implanted mice with glass micropirisms, providing optical access to the somatodendritic axis of CA1 neurons (Figures 3A and 3C).³⁷

To measure activity in CA1 pyramidal cells across the estrous cycle, two-photon imaging was performed at 12-h intervals. Since head fixation was required, mice ran on an air-floated platform, allowing them to explore a circular track (61.3 cm circumference) lined with phosphorescent visual landmarks (Figure 3D; Video S2). The experiment was otherwise conducted in darkness within an enclosed light box to eliminate the influence of distal visual cues outside the floating chamber.

Given that increased spine density during proestrus is thought to enhance dendritic excitation,¹⁴ we hypothesized that the

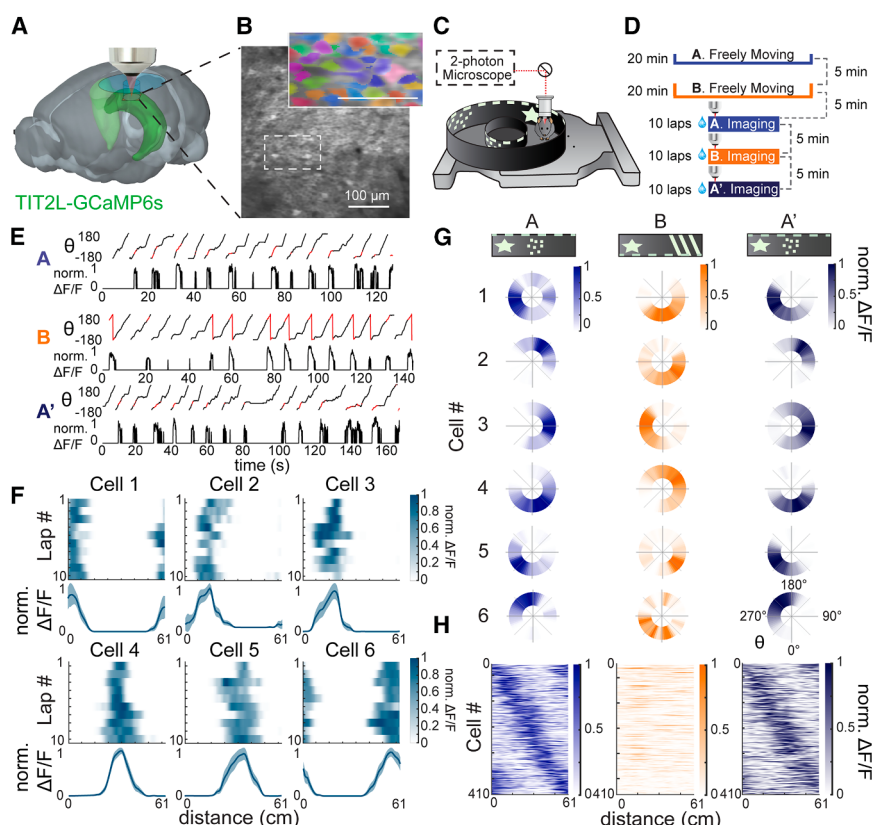


(J) Correlation between somatic and sub-ROI $\Delta F/F$ (mean \pm SEM) at increasing dendritic distances across estrous stages (LME; $***p < 0.0001$).
(K) Measurement of back-propagating action potential (bAP) propagation in proestrus. Top: somatic $\Delta F/F$ trace (blue) aligned with somatic event occurrence (logical trace, red). Bottom left: heatmap shows normalized dendritic $\Delta F/F$ as a function of distance from the soma. Note the gradually decaying dendritic response concurrent with somatic events. Bottom right: the propagation of somatic events into the primary dendrite is fit with an exponential decay function to calculate the bAP length constant.
(L) Example dendritic response of a CA1 pyramidal cell during estrus. Somatic signal, dendritic signal, and bAP length constant calculation as described in (K).
(M) Distribution of bAP length constants (mean \pm SEM) analyzed across CA1 pyramidal neurons for each estrous stage (pairwise LME, Bonferroni-corrected; $*p < 0.1$, $***p < 0.0001$).

estrous cycle would influence intrinsic excitability and somatodendritic coupling.^{52–54} Indeed, our recordings revealed significantly increased soma-dendrite coupling during proestrus and significantly decreased soma-dendrite coupling during estrus ($p < 10^{-4}$, $F(3) = 10.37$, LME, fixed effects for stage, random effects for mouse; Figures 3E–3G; Table S1C). This was found for both the correlation of $\Delta F/F$ in the somatic and dendritic compartments (Figure 3G) as well as for the conditional probability of inferred spike occurrence (Figures S4A and S4B; Table S1D). To determine whether estrous-dependent changes to somatodendritic coupling are distance dependent, we subdivided the primary dendrite into 6- μ m segments (“sub-regions of interest [ROIs]”) and re-extracted, processed, and analyzed coupling between the soma and sub-ROI along the dendrite (Figures 3H and 3I).^{52,55} All stages showed a monotonic decrease in the coupling between sub-dendritic and somatic activity with increasing distance from the soma, but there was uni-

formly higher coupling during proestrus and lower coupling during estrous ($p < 10^{-4}$, $F(3) = 212.26$, LME, fixed effects for stage, random effects for mouse; Figure 3J; Table S1C).

Back-propagating action potentials (bAPs) are critical for regenerative dendritic events^{56–60} and behavioral time scale plasticity.^{26,61,62} The observed estrous-dependent shifts in somatodendritic coupling seen during particular stages may influence bAP spread into the dendritic arbor, thereby modulating CA1 dendritic plasticity. To test this possibility, we identified potential bAP events in somatic $\Delta F/F$ traces and aligned them with corresponding dendritic responses.^{51,63} Although bAPs are typically only a few milliseconds in duration, observed transients are prolonged due to calcium and sensor kinetics, allowing for reliable observation of coupled somatodendritic activity.⁶⁴ To quantify bAP spread, we first identified somatic events, then measured the propagation of the concurrent dendritic activity into the primary dendrite (Figures 3K and 3L; see



environment B (center, orange), and back in environment A (A'; right, purple). Note similar place fields in environments A and A', but shifted place field location in environment B.
(H) Example CA1 place cell responses (normalized $\Delta F/F$) from an example recording across the three environments: A (blue), B (orange), and A' (purple). Average responses of all place cells are ordered by peak position in environment A for all three environments, cross-validated by determining peak position in odd trials and plotting even trials. Note that place field positions are aligned in environments A and A', but remap in environment B.

STAR Methods.^{55,64} The decay of the dendritic response was then fit with an exponential decay function to determine the backpropagation length constant for each cell (Figures 3K and 3L, inset plots). When analyzed by estrous stage, length constants were significantly higher in proestrus, when somatodendritic correlations were high, compared with estrus, when somatodendritic correlations were low ($p < 10^{-4}$, $F(3) = 6.55$, LME, fixed effects for stage, random effects for mouse; Figure 3M; Table S1C). To evaluate whether these effects extend to spatially tuned neurons, we repeated the analysis for place cells, defined as neurons that consistently fired in the same location along the circular track. The results were consistent for the subpopulation of place cells, with significantly greater somatodendritic coupling along the dendrite during proestrus (Figures S4C–S4G; Table S1D). These findings suggest a postsynaptic mechanism for estrous-modulated somatodendritic coupling, in which changes in synaptic density lead to increased bAP propagation into the dendritic arbor.

Place cells measured in floating environments exhibit stable responses and global remapping

Modulation of dendritic calcium dynamics has been proposed to reshape hippocampal place fields and population activity,^{61,62}

Figure 4. Changes in environmental cues induce remapping in CA1 place cells

(A) Schematic illustration of a glass cylinder implant for top-down two-photon calcium imaging of CA1 cell body layer in *CaMKIIα-Cre × TIT2L-GCaMP6s* mice.

(B) Average projection of GCaMP6s-expressing CA1 somata through the glass cylinder implant, scale bar, 100 μm. Inset, ROI selection (dashed box), with randomized color for each ROI.

(C) Schematic of head-fixed mouse in the floating chamber during two-photon imaging. The chamber walls are lined with interchangeable fluorescent visual cues, while the base has detachable textural cues to define distinct environments.

(D) Schematic of behavioral protocol, including freely moving acclimation sessions (open-top boxes) and head-fixed imaging sessions (closed boxes). For each imaging session, mice ran 10 consecutive laps, motivated by water reward. They were given 5-min rests in their home cage between sessions.

(E) Example angular position traces from the floating chamber tracking system and aligned $\Delta F/F$ transients of a single CA1 place cell across three environments (A, B, and A'). Identified $\Delta F/F$ transients are overlaid in red on the angular trace for visualization of location preference.

(F) Smoothed $\Delta F/F$ transients from six example place cells across multiple laps, with lap-averaged tuning curves below (mean ± SEM).

(G) Normalized $\Delta F/F$ of six cells as a function of angular location in environment A (left, blue), environment B (center, orange), and back in environment A (A'; right, purple).

raising the question of whether estrous cycle modulation of CA1 dendrites influences place cells. To address this, we imaged large populations of place cells across the estrous cycle in actively navigating head-fixed animals. To accomplish this in head-fixed mice, we used two floating environments with distinct visual and tactile cues to drive reliable place cell activity within an environment, as well as remapping between different environments.⁶⁵ Prior studies suggest that place cells make up 20%–30% of the total population of mouse CA1 neurons.^{37,66,67} To maximize the population of cells in the imaging field, we surgically implanted glass cylinders and performed two-photon imaging of the CA1 cell body layer, capturing large populations of place cells for further analysis (Figures 4A, 4B, S5A, and S5B; Video S3).

Since previous studies have shown that learning of specific environmental contexts peaks at approximately 21 days of exposure,⁶⁸ the mice were acclimated to the floating chamber for 21 days prior to recording, including head fixation and water reward training (Figure S5E). Different floating environments were defined by distinct patterns of phosphorescent visual cues (A: dots, B: stripes) and textural floor cues (A: foam, B: bubble wrap; Figures 4C and 4D), and experiments were carried out in a dark chamber to reduce the influence of distal cues. To

provide a common spatial reference for analysis of remapping, the water reward point had a shared visual cue (star) and textural cue (divot in base) across both environments. Before imaging, mice freely explored each environment for 20 min, with a 5-min interlude in their home cage in between exposures (Figure 4D). During imaging, mice ran ten consecutive laps in environment A, followed by a 5-min rest in their home cage. This procedure was repeated for environment B, then again in environment A (A > B > A'; Figure 4D).

To measure position during imaging, a magnetic tracking system was used to align chamber position to neural activity traces ($\Delta F/F$; Figures 4E and S4D). Calcium transients exceeding three standard deviations of the baseline were extracted and smoothed, while all other points were masked to zero to correct for slow changes in fluorescence (Figures 4E and S4D).⁶⁹ Place cells exhibited well-defined, stable place fields across laps, firing consistently at specific locations along the circular track (Figures 4E and 4F). When averaged across laps, place cells in environment A shifted their preferred angular position upon entry into environment B but returned to their original preferred position when reintroduced to environment A (A'; Figure 4G). At the population level, CA1 place cells tiled the length of the circular track, remapping between environments A and B, while maintaining stable representations when reintroduced to environment A (A'; Figures 4H, S5C, and S5D). These results demonstrate that—despite identical track geometry across environments—the visual and tactile cues provided sufficient spatial context to induce global remapping in the CA1 place cell population.⁶⁵

Place cell stability is modulated by estrous cycle stage

Having measured robust place cell responses in the floating chamber, we next examined whether within-environment place cell stability or between-environment remapping is modulated by estrous stage. Previous electrophysiological studies found that the basic firing properties of place cells remain stable across the estrous cycle.⁷⁰ Consistent with these findings, we observed no significant modulation of place cell percentage ($p = 0.2610$, Tukey HSD), place field width (full width at half maximum [FWHM]; $p = 0.1375$, $F(3) = 1.36$, LME), spatial information (bits/inferred spike; $p = 0.2457$, $F(3) = 0.92$, LME), or mean event rate ($p = 0.1196$, $F(3) = 1.13$, LME) across estrous stages (Figures S6A–S6D; Table S1E). However, lap-wise stability was significantly lower in estrus than all other stages (D: $p = 0.0029$, $F(1) = 12.22$; P: $p < 10^{-4}$, $F(1) = 54.62$; M: $p = 0.0014$, $F(1) = 13.58$, pairwise LME; Figure S6E; Table S1E). Despite this reduction, CA1 neurons still formed robust place fields during estrus (Figure S6E).

Although basic firing properties remained consistent across stages, analysis of both within-environment stability (A > A') and between-environment remapping (A > B) revealed significant estrous-cycle modulation of spatial representations. As exemplified by single-cell traces, during proestrus neurons exhibit greater stability in spatial tuning across the same environments when compared with estrus (Figure 5A). At the population level, sorting place cells by latency in environment A revealed that place cells were considerably more stable within-environment (A > A') during proestrus compared with estrus (Figure 5B).

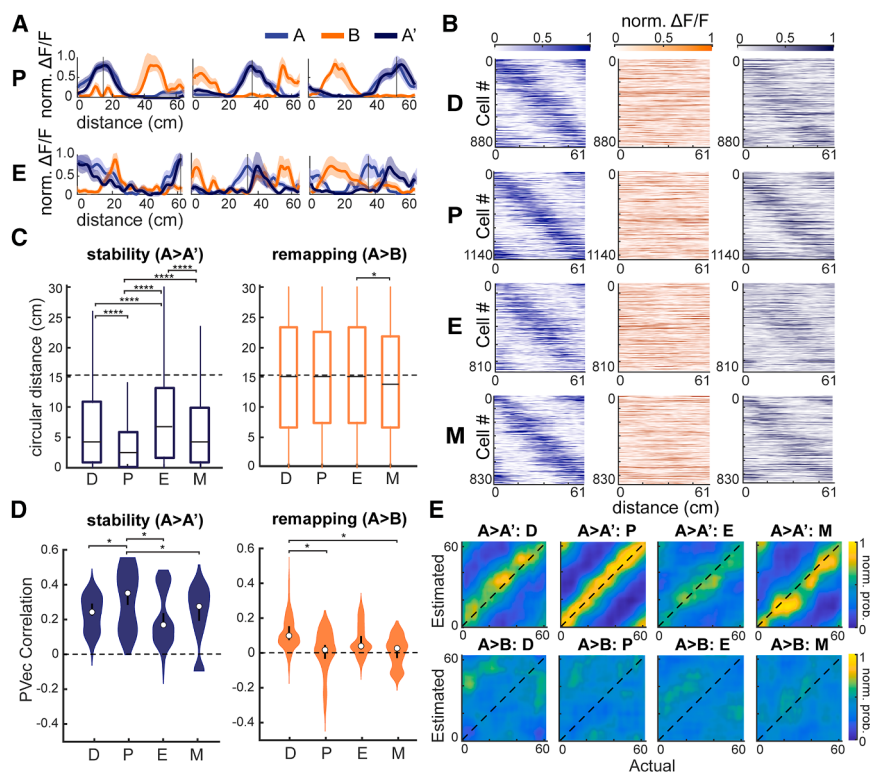
To quantify this phenomenon, we calculated the circular difference in each place cell's peak firing location within-environment (A > A'; stability; left) and between environments (A > B; remapping; right). Within-environment stability was significantly greater in proestrus and lower in estrus compared with all other estrous stages ($p < 10^{-4}$, $F(3) = 105.46$, LME, fixed effect for stage, random effects for mouse; Figure 5C, left; Table S1F). By contrast, we found only a minor difference for between-environment remapping between the estrus and metestrus stages ($p = 0.0427$, $F(3) = 2.73$, LME; Figure 5C, right; Table S1F). To confirm population-level effects, we computed the population vector (PVec) correlation, a measure of population response similarity, to assess stability and remapping across estrous stages.^{71,72} Consistent with single-cell analysis, during proestrus the place cells exhibit significantly greater stability than at any other estrous stage, as shown by non-overlapped bootstrapped 95% confidence intervals (CIs; Figure 5D). Only minor differences in remapping were observed, similar to single-cell analysis. Total moving time, speed, and anticipatory reward behavior remained consistent across the cycle (Figures S6F–S6H; Table S1E).

To further assess spatial coding fidelity, we trained a linear decoder on population-level place cell activity to predict the animal's position along the circular track.^{72,73} The decoder was trained on place cell responses in environment A, then tested on data from the same environment (A') or a different environment (B; Figure 5E). As expected, the decoded position was much more accurate in environment A' than in environment B, confirming that place cells remain stable within-environment but remap between environments (Figure 5E). Consistent with single-cell and PVec analysis, proestrus exhibited significantly lower decoder error than other stages when estimating position within-environment (A > A'), as shown by non-overlapping 95% CI (Figure S7).

Taken together, these results are the first to demonstrate that spatial representations in the hippocampus are dynamically modulated by cyclic endocrine factors, from synaptic plasticity to population-level place cell stability. This underscores a growing body of research indicating that consideration of hormonal signaling is critical to understanding the intrinsic dynamics of spatial coding and memory.

DISCUSSION

Here, we investigated the role of the murine estrous cycle on hippocampal structural and functional plasticity across synaptic, cellular, and population levels. At the synaptic level, building on previous cross-sectional studies, we found that dendritic spine density is fundamentally shaped by the estrous cycle, with a subset of proestrus-added spines becoming part of the stable synaptic population (Figures 1 and 2).^{10–14} At the cellular level, CA1 pyramidal neurons exhibited estrous-dependent dendritic activity, with greater infiltration of bAPs into the apical dendrite during the proestrus stage and less during the estrus stage (Figure 3). Finally, at the population level, we found that spatial coding was significantly more stable within the same environment (A > A') during proestrus and significantly less stable during estrus (Figure 5). These results are the first to demonstrate *in vivo* evidence that the estrous cycle modulates



dashed line indicates chance-level PVec correlation (zero), overlay indicates mean \pm bootstrapped 95% CI, and brackets indicate significant differences between stages (non-overlapping 95% CIs).

(E) Probability density plot of decoder-estimated and actual position in environment A' (A > A', top) compared with environment B (A > B, bottom). Responses are averaged across one recording per estrous stage for each of 6 mice.

hippocampal circuit function, offering a window into the role of cyclic plasticity in shaping mammalian spatial cognition.

Recent work has reshaped our understanding of synaptic plasticity's role in the formation and stability of spatial representations. Current theories of place field formation propose that CA1 place fields are driven by local dendritic activity in the form of bAPs, plateau potentials, and NMDA spikes.²⁶ These models propose that bAPs underlie non-Hebbian mechanisms supporting behavioral time scale plasticity, which causes rapid formation and stabilization of place fields.^{26,61,62} Our findings align with this framework, suggesting that the greater bAP spread observed in proestrus may contribute to place field stability at the population level.²⁶ Computational models further predict that increased excitatory dendritic input enhances place field stability, consistent with our observation that stages with higher synaptic density exhibit more stable place fields.^{73–75} An alternative possibility is that shifts in dendritic excitability could drive changes in somatodendritic coupling, which in turn influence spine dynamics. Further experiments will be necessary to distinguish between these mechanisms.

Although estrous-dependent spine turnover has been extensively studied in the hippocampus, its effects in other brain regions remain unclear. No significant estrous cycle-linked changes in spine density have been observed in the medial entorhinal cortex or somatosensory cortex.⁷⁶ However, cross-sectional synaptic

Figure 5. Place field stability is modulated by estrous cycle stage

(A) Positional tuning curves for six example place cells averaged across laps (mean \pm SEM) in the proestrus (P) and estrus (E) stages. Place fields are shown for environment A (blue), environment B (orange), and environment A' (purple). Neurons imaged during proestrus exhibit more stable place fields within-environment ($A > A'$) than neurons imaged during estrus.

(B) Average responses (normalized $\Delta F/F$) of all place cells, ordered by peak position in environment A (cross-validated), in each estrous stage (D, diestrus; P, proestrus; E, estrus; M, metestrus).

(C) Boxplots of the circular distance between place cell peak firing locations within-environment ($A > A'$; stability) or between-environment ($A > B$; remapping) in each estrous stage (horizontal line, mean; box, first and third quartiles; whiskers, maximum and minimum). The dashed line indicates chance-level circular distance (15.4 cm), and brackets indicate significant differences between stages (pairwise LME, Bonferroni-corrected; *** $p < 0.001$, ** $p < 0.01$).

(D) Violin plots of PVec correlation across estrous stages within-environment ($A > A'$; stability) and between-environment ($A > B$; remapping). Distributions were created by bootstrapping data from $N = 3,679$ cells from 6 mice over 100 iterations, sampling with replacement. A PVec correlation of zero indicates global remapping, while a PVec correlation of one indicates complete stability. The

fluctuations have been observed in the ventromedial hypothalamus,⁷⁷ prefrontal cortex,⁷⁸ and amygdala,^{79,80} although some results remain conflicting.⁸¹ Further studies investigating hormonal modulation of these regions will be crucial for understanding systemic endocrine influences on neural plasticity.

Despite the progress made by our study, there are several limitations that warrant discussion. First, we visualized dendritic spines using a well-characterized transgenic mouse line with sparse GFP expression in excitatory neurons.^{21–23,37,41–44} As with all current methods for achieving sparse neuronal expression within a broader cell type, this approach may still label a non-random subset of neurons. Second, small spine structures such as filopodia fall below our functional diffraction limit, making other techniques such as *in vivo* super-resolution stimulation emission depletion (STED) microscopy better suited for resolving these submicron structures.^{37,48} Investigating how the estrous cycle changes the growth and motility of filopodia is an exciting research direction, given the important role filopodia play in establishing new synapses.^{48,82} Third, our functional dendritic experiments were conducted using the GCaMP6s indicator, the kinetics of which are well suited for dendritic imaging over slower timescales,⁶⁴ but future studies could employ voltage imaging or *in vivo* patch clamp to capture more temporally precise dendritic dynamics. Finally, our study is ultimately observational—a critical remaining challenge is to uncover the molecular

mechanisms underlying estrous modulation of structural and functional plasticity. Classical estrogen receptors (ER α and ER β) regulate functional synapse formation in response to exogenous estradiol administration,^{1,15,24} and a subset of ER α /ER β s localize to the membranes of dendritic spines, suggesting direct involvement in synaptic signaling.^{1,9,83,84} Membrane-bound estrogen signaling is also mediated by the G-protein coupled estrogen receptor (GPER), which activates distinct secondary messenger cascades, including kinases like JNK not activated by its classical receptor counterparts.^{1,85–87} Downstream kinase activation by both classical and non-classical estradiol signaling enhances actin polymerization, promoting spine maturation, as observed during the diestrus-to-proestrus transition (Figure 2F).^{88,89} However, it remains unclear how each class of estradiol receptor, as well as receptors for other hormones like progesterone and androgens, contributes to cycle-dependent changes in hippocampal plasticity. Advances in CRISPR,⁹⁰ short hairpin RNA (shRNA),⁹¹ and transgenic technologies⁹² may pave the way for a more complete understanding of the mechanisms underlying changes in spatial coding and stability across the estrous cycle.

Given our findings, an important question to address is what are the evolutionary mechanisms underlying such significant cyclic changes to the hippocampal network? The estrous cycle is essential for reproduction, with estradiol levels peaking in proestrus, immediately prior to ovulation, then plummeting up to 15-fold in estrus.^{34,93} Behavioral studies suggest that wandering behavior increases in late proestrus, potentially enhancing mate-seeking behaviors.^{33,94} Moreover, some studies indicate that rodent navigation switches from an allocentric (map-based) to egocentric (route-based) strategy during the transition from proestrus to estrus, aligning with our findings that place cell stability is greatest during proestrus.^{95–97} However, recent deep-learning analyses of mouse behavior across the estrous cycle found that spontaneous motor activity is not strongly estrous-modulated and that individual mouse identity is significantly easier to decode than estrous stage.⁹⁸ Additionally, studies investigating the role of estradiol in performing classical spatial memory tasks (e.g., Morris water maze and radial arm maze) have produced conflicting results, with different studies showing both enhanced and impaired spatial memory after estradiol administration.^{1,99–102} Future studies will be necessary to fully understand the influence of cyclic hippocampal modulation on spatial memory and navigation behavior and to elucidate the evolutionary logic underlying cyclic changes in hippocampal plasticity.

It is important to note that the estrous cycle is often erroneously linked to the perception that female animals are more variable than males, contributing to their chronic underrepresentation in research.^{103,104} However, multiple studies have found that male rodents actually exhibit greater behavioral variability than females.^{98,105} Moreover, estradiol exerts a strong modulatory influence on the male hippocampus, where it is present at a higher concentration than in females^{1,106} and, as in females,¹⁵ induces hippocampal synaptogenesis.^{88,107} Hormonal cycles are also not exclusive to females. For example, circadian rhythms are ubiquitous among mammals, with coupled steroid hormone concentration typically peaking in the morning and declining in the evening.¹⁰⁸ Male mice also exhibit cyclic fluctu-

ations of testosterone, progesterone, and cortisol throughout the day.¹⁰⁹ However, unlike the 4–5 day cycle of female mice, male hormone fluctuations occur on a shorter timescale, making it difficult to capture cyclic plasticity changes, and vaginal cytology is not an option for non-invasive staging of hormonal state. Future studies using new technologies for plasma hormone assessment^{110,111} may provide insight into how gonadal hormones influence hippocampal circuitry in males.

Our findings demonstrate that naturally cycling endocrine factors are robust modulators of spatial memory circuits, shaping hippocampal structure and function on a previously unpreceded scale. These results highlight the need to consider hormonal influences in neuroscience research and pave the way for future studies exploring the interplay between endocrine rhythms, synaptic plasticity, and cognition.

RESOURCE AVAILABILITY

Lead contact

Requests for further information and for reagents and resources should be directed to and will be fulfilled by the lead contact, Michael J. Goard (michaelgoard@ucsb.edu).

Materials availability

This study did not generate new, unique reagents.

Data and code availability

Spine morphology images and processed calcium imaging traces generated in this study have been deposited in a public repository (Mendeley Data: <https://www.doi.org/10.17632/fwd9b5jv9h.1>). The analysis code used to measure spine morphology (GitHub: <https://www.doi.org/10.5281/zenodo.15200450>), dendritic activity (GitHub: <https://www.doi.org/10.5281/zenodo.15200438>), and place cell dynamics (GitHub: <https://www.doi.org/10.5281/zenodo.15200440>) is publicly available. Any additional information required to reanalyze the data reported in this paper is available from the lead contact upon request.

ACKNOWLEDGMENTS

We would like to thank Ikuko Smith, Catherine Wooley, and Karyn Frick for discussion of the results. We would also like to thank Claire Cady, Nathaniel Bailey, and Yifan Xu for assisting in cytology collection and staging and Mounami Kayitha for assisting in data analysis. This work was supported by a grant from the NIH (F99 NS139514) to N.S.W. and grants from the NIH (R01 NS121919), NSF (NeuroNex 1934288), and Whitehall Foundation (2022-05-009) to M.J.G.

AUTHOR CONTRIBUTIONS

Conceptualization, N.S.W., W.T.R., E.G.J., and M.J.G.; methodology, N.S.W., W.T.R., M.K., and M.J.G.; investigation, N.S.W. and M.J.G.; visualization, N.S.W. and M.J.G.; funding acquisition, N.S.W. and M.J.G.; project administration, M.J.G.; supervision, M.J.G.; writing – original draft, N.S.W. and M.J.G.; writing – review and editing, N.S.W., W.T.R., E.G.J., and M.J.G.

DECLARATION OF INTERESTS

The authors declare no competing interests.

STAR★METHODS

Detailed methods are provided in the online version of this paper and include the following:

- KEY RESOURCES TABLE
- EXPERIMENTAL MODEL AND STUDY PARTICIPANT DETAILS
- METHOD DETAILS
 - Estrous cycle staging
 - Surgical procedures
 - Floating chamber setup, training, and recording
 - Two-photon imaging
 - Two-photon image post-processing
 - Spine imaging data analysis
 - Dendritic calcium imaging data analysis
 - Population calcium imaging data analysis
 - Histology
- QUANTIFICATION AND STATISTICAL ANALYSIS

SUPPLEMENTAL INFORMATION

Supplemental information can be found online at <https://doi.org/10.1016/j.neuron.2025.04.014>.

Received: July 24, 2024

Revised: February 21, 2025

Accepted: April 16, 2025

Published: May 13, 2025

REFERENCES

1. Taxier, L.R., Gross, K.S., and Frick, K.M. (2020). Oestradiol as a neuro-modulator of learning and memory. *Nat. Rev. Neurosci.* 21, 535–550. <https://doi.org/10.1038/s41583-020-0362-7>.
2. Brinton, R.D., Thompson, R.F., Foy, M.R., Baudry, M., Wang, J., Finch, C.E., Morgan, T.E., Pike, C.J., Mack, W.J., Stanczyk, F.Z., et al. (2008). Progesterone receptors: Form and function in brain. *Front. Neuroendocrinol.* 29, 313–339. <https://doi.org/10.1016/j.yfrne.2008.02.001>.
3. McEwen, B., Akama, K., Alves, S., Brake, W.G., Bulloch, K., Lee, S., Li, C., Yuen, G., and Milner, T.A. (2001). Tracking the estrogen receptor in neurons: Implications for estrogen-induced synapse formation. *Proc. Natl. Acad. Sci. USA* 98, 7093–7100. <https://doi.org/10.1073/pnas.121146898>.
4. O'Keefe, J., and Nadel, L. (1978). *The Hippocampus as a Cognitive Map* (Clarendon Press; Oxford University Press).
5. Nieh, E.H., Schottendorf, M., Freeman, N.W., Low, R.J., Lewallen, S., Koay, S.A., Pinto, L., Gauthier, J.L., Brody, C.D., and Tank, D.W. (2021). Geometry of abstract learned knowledge in the hippocampus. *Nature* 595, 80–84. <https://doi.org/10.1038/s41586-021-03652-7>.
6. Tonegawa, S., Liu, X., Ramirez, S., and Redondo, R. (2015). Memory Engram Cells Have Come of Age. *Neuron* 87, 918–931. <https://doi.org/10.1016/j.neuron.2015.08.002>.
7. Pritschet, L., Santander, T., Taylor, C.M., Layher, E., Yu, S., Miller, M.B., Grafton, S.T., and Jacobs, E.G. (2020). Functional reorganization of brain networks across the human menstrual cycle. *NeuroImage* 220, 117091. <https://doi.org/10.1016/j.neuroimage.2020.117091>.
8. Kato, A., Hojo, Y., Higo, S., Komatsuzaki, Y., Murakami, G., Yoshino, H., Uebayashi, M., and Kawato, S. (2013). Female hippocampal estrogens have a significant correlation with cyclic fluctuation of hippocampal spines. *Front. Neural Circuits* 7, 149. <https://doi.org/10.3389/fncir.2013.00149>.
9. Remage-Healey, L., Saldanha, C.J., and Schlinger, B.A. (2011). Estradiol Synthesis and Action at the Synapse: Evidence for "Synaptocrine" Signaling. *Front. Endocrinol.* 2, 28. <https://doi.org/10.3389/fendo.2011.00028>.
10. Woolley, C.S., Gould, E., Frankfurt, M., and McEwen, B.S. (1990). Naturally occurring fluctuation in dendritic spine density on adult hippocampal pyramidal neurons. *J. Neurosci.* 10, 4035–4039. <https://doi.org/10.1523/JNEUROSCI.10-12-04035.1990>.
11. Gould, E., Woolley, C.S., Frankfurt, M., and McEwen, B.S. (1990). Gonadal steroids regulate dendritic spine density in hippocampal pyramidal cells in adulthood. *J. Neurosci.* 10, 1286–1291. <https://doi.org/10.1523/JNEUROSCI.10-04-01286.1990>.
12. Woolley, C.S., and McEwen, B.S. (1992). Estradiol mediates fluctuation in hippocampal synapse density during the estrous cycle in the adult rat. *J. Neurosci.* 12, 2549–2554. <https://doi.org/10.1523/JNEUROSCI.12-07-02549.1992>.
13. Woolley, C.S., and McEwen, B.S. (1993). Roles of estradiol and progesterone in regulation of hippocampal dendritic spine density during the estrous cycle in the rat. *J. Comp. Neurol.* 336, 293–306. <https://doi.org/10.1002/cne.903360210>.
14. Woolley, C.S., and McEwen, B.S. (1994). Estradiol regulates hippocampal dendritic spine density via an N-methyl-D-aspartate receptor-dependent mechanism. *J. Neurosci.* 14, 7680–7687. <https://doi.org/10.1523/JNEUROSCI.14-12-07680.1994>.
15. Woolley, C.S., Weiland, N.G., McEwen, B.S., and Schwartzkroin, P.A. (1997). Estradiol increases the sensitivity of hippocampal CA1 pyramidal cells to NMDA receptor-mediated synaptic input: correlation with dendritic spine density. *J. Neurosci.* 17, 1848–1859. <https://doi.org/10.1523/JNEUROSCI.17-05-01848.1997>.
16. Leranth, C., Shanabrough, M., and Redmond, D.E., Jr. (2002). Gonadal hormones are responsible for maintaining the integrity of spine synapses in the CA1 hippocampal subfield of female nonhuman primates. *J. Comp. Neurol.* 447, 34–42. <https://doi.org/10.1002/cne.10230>.
17. Vasudevan, N., and Pfaff, D.W. (2008). Non-genomic actions of estrogens and their interaction with genomic actions in the brain. *Front. Neuroendocrinol.* 29, 238–257. <https://doi.org/10.1016/j.yfrne.2007.08.003>.
18. Zhao, Z., Fan, L., and Frick, K.M. (2010). Epigenetic alterations regulate estradiol-induced enhancement of memory consolidation. *Proc. Natl. Acad. Sci. USA* 107, 5605–5610. <https://doi.org/10.1073/pnas.0910578107>.
19. Taylor, C.M., Pritschet, L., Olsen, R.K., Layher, E., Santander, T., Grafton, S.T., and Jacobs, E.G. (2020). Progesterone shapes medial temporal lobe volume across the human menstrual cycle. *NeuroImage* 220, 117125. <https://doi.org/10.1016/j.neuroimage.2020.117125>.
20. Zsido, R.G., Williams, A.N., Barth, C., Serio, B., Kurth, L., Mildner, T., Trampel, R., Beyer, F., Witte, A.V., Villringer, A., et al. (2023). Ultra-high-field 7T MRI reveals changes in human medial temporal lobe volume in female adults during menstrual cycle. *Nat. Mental Health* 1, 761–771. <https://doi.org/10.1038/s44220-023-00125-w>.
21. Attardo, A., Fitzgerald, J.E., and Schnitzer, M.J. (2015). Impermanence of dendritic spines in live adult CA1 hippocampus. *Nature* 523, 592–596. <https://doi.org/10.1038/nature14467>.
22. Trachtenberg, J.T., Chen, B.E., Knott, G.W., Feng, G., Sanes, J.R., Welker, E., and Svoboda, K. (2002). Long-term *in vivo* imaging of experience-dependent synaptic plasticity in adult cortex. *Nature* 420, 788–794. <https://doi.org/10.1038/nature01273>.
23. Shao, L.-X., Liao, C., Gregg, I., Davoudian, P.A., Savalia, N.K., Delagarza, K., and Kwan, A.C. (2021). Psilocybin induces rapid and persistent growth of dendritic spines in frontal cortex *in vivo*. *Neuron* 109, 2535–2544.e4. <https://doi.org/10.1016/j.neuron.2021.06.008>.
24. Yankova, M., Hart, S.A., and Woolley, C.S. (2001). Estrogen increases synaptic connectivity between single presynaptic inputs and multiple postsynaptic CA1 pyramidal cells: A serial electron-microscopic study. *Proc. Natl. Acad. Sci. USA* 98, 3525–3530. <https://doi.org/10.1073/pnas.051624598>.
25. Wilson, M.A., and McNaughton, B.L. (1993). Dynamics of the hippocampal ensemble code for space. *Science* 261, 1055–1058. <https://doi.org/10.1126/science.8351520>.

26. Sheffield, M.E., and Dombbeck, D.A. (2019). Dendritic mechanisms of hippocampal place field formation. *Curr. Opin. Neurobiol.* 54, 1–11. <https://doi.org/10.1016/j.conb.2018.07.004>.
27. Muller, R.U., and Kubie, J.L. (1987). The effects of changes in the environment on the spatial firing of hippocampal complex-spike cells. *J. Neurosci.* 7, 1951–1968. <https://doi.org/10.1523/JNEUROSCI.07-07-01951.1987>.
28. Fyhn, M., Hafting, T., Treves, A., Moser, M.-B., and Moser, E.I. (2007). Hippocampal remapping and grid realignment in entorhinal cortex. *Nature* 446, 190–194. <https://doi.org/10.1038/nature05601>.
29. Sosa, M., Plitt, M.H., and Giocomo, L.M. (2024). Hippocampal sequences span experience relative to rewards. Preprint at bioRxiv, 2023.12.27.573490. <https://doi.org/10.1101/2023.12.27.573490>.
30. Liberti, W.A., Schmid, T.A., Forli, A., Snyder, M., and Yartsev, M.M. (2022). A stable hippocampal code in freely flying bats. *Nature* 604, 98–103. <https://doi.org/10.1038/s41586-022-04560-0>.
31. Julian, J.B., and Doeller, C.F. (2021). Remapping and realignment in the human hippocampal formation predict context-dependent spatial behavior. *Nat. Neurosci.* 24, 863–872. <https://doi.org/10.1038/s41593-021-00835-3>.
32. Kentros, C., Hargreaves, E., Hawkins, R.D., Kandel, E.R., Shapiro, M., and Muller, R.V. (1998). Abolition of Long-Term Stability of New Hippocampal Place Cell Maps by NMDA Receptor Blockade. *Science* 280, 2121–2126. <https://doi.org/10.1126/science.280.5372.2121>.
33. Allen, E. (1922). The oestrous cycle in the mouse. *Am. J. Anat.* 30, 297–371. <https://doi.org/10.1002/aja.1000300303>.
34. Goldman, J.M., Murr, A.S., and Cooper, R.L. (2007). The rodent estrous cycle: characterization of vaginal cytology and its utility in toxicological studies. *Birth Defects Res. B Dev. Reprod. Toxicol.* 80, 84–97. <https://doi.org/10.1002/bdrb.20106>.
35. Byers, S.L., Wiles, M.V., Dunn, S.L., and Taft, R.A. (2012). Mouse estrous cycle identification tool and images. *PLoS One* 7, e35538. <https://doi.org/10.1371/journal.pone.0035538>.
36. Wolcott, N.S., Sit, K.K., Raimondi, G., Hodges, T., Shansky, R.M., Galea, L.A.M., Ostroff, L.E., and Goard, M.J. (2022). Automated classification of estrous stage in rodents using deep learning. *Sci. Rep.* 12, 17685. <https://doi.org/10.1038/s41598-022-22392-w>.
37. Redman, W.T., Wolcott, N.S., Montelisciani, L., Luna, G., Marks, T.D., Sit, K.K., Yu, C.H., Smith, S., and Goard, M.J. (2022). Long-term transverse imaging of the hippocampus with glass microscopes. *eLife* 11, e75391. <https://doi.org/10.7554/eLife.75391>.
38. Sano, K., Matsuda, S., Tohyama, S., Komura, D., Shimizu, E., and Sutoh, C. (2020). Deep learning-based classification of the mouse estrous cycle stages. *Sci. Rep.* 10, 11714. <https://doi.org/10.1038/s41598-020-68611-0>.
39. Dombbeck, D.A., Harvey, C.D., Tian, L., Looger, L.L., and Tank, D.W. (2010). Functional imaging of hippocampal place cells at cellular resolution during virtual navigation. *Nat. Neurosci.* 13, 1433–1440. <https://doi.org/10.1038/nn.2648>.
40. Ramón y Cajal, S. (1909). *Histologie du Système Nerveux de l'Homme & Des Vertébrés* (Maloine).
41. Feng, G., Mellor, R.H., Bernstein, M., Keller-Peck, C., Nguyen, Q.T., Wallace, M., Nerbonne, J.M., Lichtman, J.W., and Sanes, J.R. (2000). Imaging neuronal subsets in transgenic mice expressing multiple spectral variants of GFP. *Neuron* 28, 41–51. [https://doi.org/10.1016/s0896-6273\(00\)00084-2](https://doi.org/10.1016/s0896-6273(00)00084-2).
42. Grutzendler, J., Kasthuri, N., and Gan, W.-B. (2002). Long-term dendritic spine stability in the adult cortex. *Nature* 420, 812–816. <https://doi.org/10.1038/nature01276>.
43. Tønnesen, J., Katona, G., Rózsa, B., and Nägerl, U.V. (2014). Spine neck plasticity regulates compartmentalization of synapses. *Nat. Neurosci.* 17, 678–685. <https://doi.org/10.1038/nn.3682>.
44. Bedbrook, C.N., Deverman, B.E., and Gradinaru, V. (2018). Viral Strategies for Targeting the Central and Peripheral Nervous Systems. *Annu. Rev. Neurosci.* 41, 323–348. <https://doi.org/10.1146/annurev-neuro-080317-062048>.
45. Chang, F.L., and Greenough, W.T. (1984). Transient and enduring morphological correlates of synaptic activity and efficacy change in the rat hippocampal slice. *Brain Res.* 309, 35–46. [https://doi.org/10.1016/0006-8993\(84\)91008-4](https://doi.org/10.1016/0006-8993(84)91008-4).
46. Rodriguez, A., Ehlenberger, D.B., Dickstein, D.L., Hof, P.R., and Wearne, S. L. (2008). Automated Three-Dimensional Detection and Shape Classification of Dendritic Spines from Fluorescence Microscopy Images. *PLoS One* 3, e1997. <https://doi.org/10.1371/journal.pone.0001997>.
47. Son, J., Song, S., Lee, S., Chang, S., and Kim, M. (2011). Morphological change tracking of dendritic spines based on structural features. *J. Microsc.* 241, 261–272. <https://doi.org/10.1111/j.1365-2818.2010.03427.x>.
48. Vardalaki, D., Chung, K., and Harnett, M.T. (2022). Filopodia are a structural substrate for silent synapses in adult neocortex. *Nature* 612, 323–327. <https://doi.org/10.1038/s41586-022-05483-6>.
49. Pfeiffer, T., Poll, S., Bancelin, S., Angibaud, J., Inavalli, V.K., Keppler, K., Mittag, M., Fuhrmann, M., and Nägerl, U.V. (2018). Chronic 2P-STED imaging reveals high turnover of dendritic spines in the hippocampus *in vivo*. *eLife* 7, e34700. <https://doi.org/10.7554/eLife.34700>.
50. Yang, G., Pan, F., and Gan, W.-B. (2009). Stably maintained dendritic spines are associated with lifelong memories. *Nature* 462, 920–924. <https://doi.org/10.1038/nature08577>.
51. Chen, T.-W., Wardill, T.J., Sun, Y., Pulver, S.R., Renninger, S.L., Baohan, A., Schreiter, E.R., Kerr, R.A., Orger, M.B., Jayaraman, V., et al. (2013). Ultrasensitive fluorescent proteins for imaging neuronal activity. *Nature* 499, 295–300. <https://doi.org/10.1038/nature12354>.
52. O'Hare, J.K., Gonzalez, K.C., Herrlinger, S.A., Hirabayashi, Y., Hewitt, V. L., Blockus, H., Szoboszlay, M., Rolotti, S.V., Geiller, T.C., Negrean, A., et al. (2022). Compartment-specific tuning of dendritic feature selectivity by intracellular Ca²⁺ release. *Science* 375, eabm1670. <https://doi.org/10.1126/science.abm1670>.
53. Beaulieu-Laroche, L., Toloza, E.H.S., Brown, N.J., and Harnett, M.T. (2019). Widespread and Highly Correlated Somato-dendritic Activity in Cortical Layer 5 Neurons. *Neuron* 103, 235–241.e4. <https://doi.org/10.1016/j.neuron.2019.05.014>.
54. Francioni, V., Padamsey, Z., and Rochefort, N.L. (2019). High and asymmetric somato-dendritic coupling of V1 layer 5 neurons independent of visual stimulation and locomotion. *eLife* 8, e49145. <https://doi.org/10.7554/eLife.49145>.
55. Jia, H., Rochefort, N.L., Chen, X., and Konnerth, A. (2010). Dendritic organization of sensory input to cortical neurons *in vivo*. *Nature* 464, 1307–1312. <https://doi.org/10.1038/nature08947>.
56. Helmchen, F., Svoboda, K., Denk, W., and Tank, D.W. (1999). In vivo dendritic calcium dynamics in deep-layer cortical pyramidal neurons. *Nat. Neurosci.* 2, 989–996. <https://doi.org/10.1038/14788>.
57. Buzsáki, G., and Kandel, A. (1998). Somadendritic Backpropagation of Action Potentials in Cortical Pyramidal Cells of the Awake Rat. *J. Neurophysiol.* 79, 1587–1591. <https://doi.org/10.1152/jn.1998.79.3.1587>.
58. Svoboda, K., Helmchen, F., Denk, W., and Tank, D.W. (1999). Spread of dendritic excitation in layer 2/3 pyramidal neurons in rat barrel cortex *in vivo*. *Nat. Neurosci.* 2, 65–73. <https://doi.org/10.1038/4569>.
59. Magee, J.C., and Johnston, D.A. (1997). A Synaptically Controlled, Associative Signal for Hebbian Plasticity in Hippocampal Neurons. *Science* 275, 209–213. <https://doi.org/10.1126/science.275.5297.209>.
60. Stuart, G.J., and Sakmann, B. (1994). Active propagation of somatic action potentials into neocortical pyramidal cell dendrites. *Nature* 367, 69–72. <https://doi.org/10.1038/367069a0>.

61. Milstein, A.D., Li, Y., Bittner, K.C., Grienberger, C., Soltesz, I., Magee, J.C., and Romani, S. (2021). Bidirectional synaptic plasticity rapidly modifies hippocampal representations. *eLife* 10, e73046. <https://doi.org/10.7554/eLife.73046>.
62. Bittner, K.C., Milstein, A.D., Grienberger, C., Romani, S., and Magee, J.C. (2017). Behavioral time scale synaptic plasticity underlies CA1 place fields. *Science* 357, 1033–1036. <https://doi.org/10.1126/science.aan3846>.
63. Yu, Y., Adsit, L.M., and Smith, I.T. (2024). Comprehensive software suite for functional analysis and synaptic input mapping of dendritic spines imaged in vivo. *Neurophotonics* 11, 024307. <https://doi.org/10.1117/1.NPh.11.2.024307>.
64. Ali, F., and Kwan, A.C. (2020). Interpreting in vivo calcium signals from neuronal cell bodies, axons, and dendrites: a review. *Neurophotonics* 7, 011402. <https://doi.org/10.1117/1.NPh.7.1.011402>.
65. Go, M.A., Rogers, J., Gava, G.P., Davey, C.E., Prado, S., Liu, Y., and Schultz, S.R. (2021). Place Cells in Head-Fixed Mice Navigating a Floating Real-World Environment. *Front. Cell. Neurosci.* 15, 618658. <https://doi.org/10.3389/fncel.2021.618658>.
66. Ziv, Y., Burns, L.D., Cocker, E.D., Hamel, E.O., Ghosh, K.K., Kitch, L.J., El Gamal, A., and Schnitzer, M.J. (2013). Long-term dynamics of CA1 hippocampal place codes. *Nat. Neurosci.* 16, 264–266. <https://doi.org/10.1038/nn.3329>.
67. Meshulam, L., Gauthier, J.L., Brody, C.D., Tank, D.W., and Bialek, W. (2017). Collective Behavior of Place and Non-place Neurons in the Hippocampal Network. *Neuron* 96, 1178–1191.e4. <https://doi.org/10.1016/j.neuron.2017.10.027>.
68. Lever, C., Wills, T., Cacucci, F., Burgess, N., and O'Keefe, J. (2002). Long-term plasticity in hippocampal place-cell representation of environmental geometry. *Nature* 416, 90–94. <https://doi.org/10.1038/416090a>.
69. Hainmueller, T., and Bartos, M. (2018). Parallel emergence of stable and dynamic memory engrams in the hippocampus. *Nature* 558, 292–296. <https://doi.org/10.1038/s41586-018-0191-2>.
70. Tropp, J., Figueiredo, C.M., and Markus, E.J. (2005). Stability of hippocampal place cell activity across the rat estrous cycle. *Hippocampus* 15, 154–165. <https://doi.org/10.1002/hipo.20042>.
71. Jun, H., Bramian, A., Soma, S., Saito, T., Saido, T.C., and Igashiki, K.M. (2020). Disrupted Place Cell Remapping and Impaired Grid Cells in a Knockin Model of Alzheimer's Disease. *Neuron* 107, 1095–1112.e6. <https://doi.org/10.1016/j.neuron.2020.06.023>.
72. Leutgeb, S., Leutgeb, J.K., Barnes, C.A., Moser, E.I., McNaughton, B.L., and Moser, M.B. (2005). Independent codes for spatial and episodic memory in hippocampal neuronal ensembles. *Science* 309, 619–623. <https://doi.org/10.1126/science.1114037>.
73. Pedrosa, V., and Clopath, C. (2020). The interplay between somatic and dendritic inhibition promotes the emergence and stabilization of place fields. *PLoS Comput. Biol.* 16, e1007955. <https://doi.org/10.1371/journal.pcbi.1007955>.
74. Geiller, T., Sadeh, S., Rolotti, S.V., Blockus, H., Vancura, B., Negrean, A., Murray, A.J., Rózsa, B., Polleux, F., Clopath, C., et al. (2022). Local circuit amplification of spatial selectivity in the hippocampus. *Nature* 601, 105–109. <https://doi.org/10.1038/s41586-021-04169-9>.
75. Mazzara, C., and Migliore, M. (2023). A realistic computational model for the formation of a Place Cell. *Sci. Rep.* 13, 21763. <https://doi.org/10.1038/s41598-023-48183-5>.
76. Alexander, B.H., Barnes, H.M., Trimmer, E., Davidson, A.M., Ogola, B.O., Lindsey, S.H., and Mostany, R. (2018). Stable Density and Dynamics of Dendritic Spines of Cortical Neurons Across the Estrous Cycle While Expressing Differential Levels of Sensory-Evoked Plasticity. *Front. Mol. Neurosci.* 11, 83. <https://doi.org/10.3389/fnmol.2018.00083>.
77. Frankfurt, M., Gould, E., Woolley, C.S., and McEwen, B.S. (1990). Gonadal Steroids Modify Dendritic Spine Density in Ventromedial Hypothalamic Neurons: A Golgi Study in the Adult Rat. *Neuroendocrinology* 51, 530–535. <https://doi.org/10.1159/000125387>.
78. Tang, Y., Janssen, W.G.M., Hao, J., Roberts, J.A., McKay, H., Lasley, B., Allen, P.B., Greengard, P., Rapp, P.R., Kordower, J.H., et al. (2004). Estrogen Replacement Increases Spinophilin-immunoreactive Spine Number in the Prefrontal Cortex of Female Rhesus Monkeys. *Cereb. Cortex* 14, 215–223. <https://doi.org/10.1093/cercor/bhg121>.
79. de Castilhos, J., Forti, C.D., Achaval, M., and Rasia-Filho, A.A. (2008). Dendritic spine density of posterodorsal medial amygdala neurons can be affected by gonadectomy and sex steroid manipulations in adult rats: a Golgi study. *Brain Res.* 1240, 73–81. <https://doi.org/10.1016/j.brainres.2008.09.002>.
80. Rasia-Filho, A.A., Dalpian, F., Menezes, I.C., Brusco, J., Moreira, J.E., and Cohen, R.S. (2012). Dendritic spines of the medial amygdala: plasticity, density, shape, and subcellular modulation by sex steroids. *Histol. Histopathol.* 27, 985–1011. <https://doi.org/10.14670/HH-27.985>.
81. Brandt, N., Löffler, T., Fester, L., and Rune, G.M. (2020). Sex-specific features of spine densities in the hippocampus. *Sci. Rep.* 10, 11405. <https://doi.org/10.1038/s41598-020-68371-x>.
82. Ziv, N.E., and Smith, S.J. (1996). Evidence for a role of dendritic filopodia in synaptogenesis and spine formation. *Neuron* 17, 91–102. [https://doi.org/10.1016/s0896-6273\(00\)80283-4](https://doi.org/10.1016/s0896-6273(00)80283-4).
83. Ábrahám, I.M., Todman, M.G., Korach, K.S., and Herbison, A.E. (2004). Critical In Vivo Roles for Classical Estrogen Receptors in Rapid Estrogen Actions on Intracellular Signaling in Mouse Brain. *Endocrinology* 145, 3055–3061. <https://doi.org/10.1210/en.2003-1676>.
84. Razandi, M., Pedram, A., Park, S.T., and Levin, E.R. (2003). Proximal Events in Signaling by Plasma Membrane Estrogen Receptors. *J. Biol. Chem.* 278, 2701–2712. <https://doi.org/10.1074/jbc.M205692200>.
85. Thomas, P., Pang, Y., Filardo, E.J., and Dong, J. (2005). Identity of an Estrogen Membrane Receptor Coupled to a G Protein in Human Breast Cancer Cells. *Endocrinology* 146, 624–632. <https://doi.org/10.1210/en.2004-1064>.
86. Revankar, C.M., Cimino, D.F., Sklar, L.A., Arterburn, J.B., and Prossnitz, E.R. (2005). A Transmembrane Intracellular Estrogen Receptor Mediates Rapid Cell Signaling. *Science* 307, 1625–1630. <https://doi.org/10.1126/science.1106943>.
87. Sherrin, T., Blank, T., and Todorovic, C. (2011). c-Jun N-terminal kinases in memory and synaptic plasticity. *Rev. Neurosci.* 22, 403–410. <https://doi.org/10.1515/RNS.2011.032>.
88. Kramár, E.A., Chen, L.Y., Brandon, N.J., Rex, C.S., Liu, F., Gall, C.M., and Lynch, G. (2009). Cytoskeletal Changes Underlie Estrogen's Acute Effects on Synaptic Transmission and Plasticity. *J. Neurosci.* 29, 12982–12993. <https://doi.org/10.1523/JNEUROSCI.3059-09.2009>.
89. Sanchez, A.M., Flamini, M.I., Polak, K., Palla, G., Spina, S., Mannella, P., Genazzani, A.D., and Simoncini, T. (2012). Actin Cytoskeleton Remodelling by Sex Steroids in Neurones. *J. Neuroendocrinol.* 24, 195–201. <https://doi.org/10.1111/j.1365-2826.2011.02258.x>.
90. Marciano, S., Ionescu, T.M., Saw, R.S., Cheong, R.Y., Kirik, D., Maurer, A., Pichler, B.J., and Herfert, K. (2022). Combining CRISPR-Cas9 and brain imaging to study the link from genes to molecules to networks. *Proc. Natl. Acad. Sci. USA* 119, e2122552119. <https://doi.org/10.1073/pnas.2122552119>.
91. Golden, C.E.M., Martin, A.C., Kaur, D., Mah, A., Levy, D.H., Yamaguchi, T., Lasek, A.W., Lin, D., Aoki, C., and Constantinople, C.M. (2024). Estrogenic control of reward prediction errors and reinforcement learning. Preprint at bioRxiv, 2023.12.09.570945. <https://doi.org/10.1101/2023.12.09.570945>.
92. Feng, Y., Manka, D., Wagner, K.-U., and Khan, S.A. (2007). Estrogen receptor- α expression in the mammary epithelium is required for ductal and alveolar morphogenesis in mice. *Proc. Natl. Acad. Sci. USA* 104, 14718–14723. <https://doi.org/10.1073/pnas.0706933104>.

93. Nilsson, M.E., Vandenput, L., Tivesten, Å., Norlén, A.K., Lagerquist, M.K., Windahl, S.H., Börjesson, A.E., Farman, H.H., Poutanen, M., Benrick, A., et al. (2015). Measurement of a Comprehensive Sex Steroid Profile in Rodent Serum by High-Sensitive Gas Chromatography-Tandem Mass Spectrometry. *Endocrinology* 156, 2492–2502. <https://doi.org/10.1210/en.2014-1890>.
94. Steiner, M., Katz, R.J., Baldighi, G., and Carroll, B.J. (1981). Motivated behavior and the estrous cycle in rats. *Psychoneuroendocrinology* 6, 81–90. [https://doi.org/10.1016/0306-4530\(81\)90051-2](https://doi.org/10.1016/0306-4530(81)90051-2).
95. Galea, L.A.M., Kavaliers, M., and Ossenkopp, K.P. (1996). Sexually Dimorphic Spatial Learning in Meadow Voles *Microtus Pennsylvanicus* and Deer Mice *Peromyscus maniculatus*. *J. Exp. Biol.* 199, 195–200. <https://doi.org/10.1242/jeb.199.1.195>.
96. Korol, D.L., Malin, E.L., Borden, K.A., Busby, R.A., and Couper-Leo, J. (2004). Shifts in preferred learning strategy across the estrous cycle in female rats. *Horm. Behav.* 45, 330–338. <https://doi.org/10.1016/j.yhbeh.2004.01.005>.
97. Qiu, L.R., Germann, J., Spring, S., Alm, C., Vousden, D.A., Palmert, M.R., and Lerch, J.P. (2013). Hippocampal volumes differ across the mouse estrous cycle, can change within 24 hours, and associate with cognitive strategies. *NeuroImage* 83, 593–598. <https://doi.org/10.1016/j.neuroimage.2013.06.074>.
98. Levy, D.R., Hunter, N., Lin, S., Robinson, E.M., Gillis, W., Conlin, E.B., Anyoha, R., Shansky, R.M., and Datta, S.R. (2023). Mouse spontaneous behavior reflects individual variation rather than estrous state. *Curr. Biol.* 33, 1358–1364.e4. <https://doi.org/10.1016/j.cub.2023.02.035>.
99. Warren, S.G., and Juraska, J.M. (1997). Spatial and nonspatial learning across the rat estrous cycle. *Behav. Neurosci.* 111, 259–266. <https://doi.org/10.1037/0735-7044.111.2.259>.
100. Berry, B., McMahan, R., and Gallagher, M. (1997). Spatial learning and memory at defined points of the estrous cycle: effects on performance of a hippocampal-dependent task. *Behav. Neurosci.* 111, 267–274. <https://doi.org/10.1037/0735-7044.111.2.267>.
101. Frick, K.M., and Berger-Sweeney, J. (2001). Spatial reference memory and neocortical neurochemistry vary with the estrous cycle in C57BL/6 mice. *Behav. Neurosci.* 115, 229–237. <https://doi.org/10.1037/0735-7044.115.1.229>.
102. Pompili, A., Tomaz, C., Arnone, B., Tavares, M.C., and Gasbarri, A. (2010). Working and reference memory across the estrous cycle of rat: A long-term study in gonadally intact females. *Behav. Brain Res.* 213, 10–18. <https://doi.org/10.1016/j.bbr.2010.04.018>.
103. Shansky, R.M., and Murphy, A.Z. (2021). Considering sex as a biological variable will require a global shift in science culture. *Nat. Neurosci.* 24, 457–464. <https://doi.org/10.1038/s41593-021-00806-8>.
104. Woitowich, N.C., Beery, A., and Woodruff, T. (2020). A 10-year follow-up study of sex inclusion in the biological sciences. *eLife* 9, e56344. <https://doi.org/10.7554/eLife.56344>.
105. Beery, A.K. (2018). Inclusion of females does not increase variability in rodent research studies. *Curr. Opin. Behav. Sci.* 23, 143–149. <https://doi.org/10.1016/j.cobeha.2018.06.016>.
106. Hojo, Y., Hattori, T.A., Enami, T., Furukawa, A., Suzuki, K., Ishii, H.T., Mukai, H., Morrison, J.H., Janssen, W.G.M., Kominami, S., et al. (2004). Adult male rat hippocampus synthesizes estradiol from pregnenolone by cytochromes P45017 α and P450 aromatase localized in neurons. *Proc. Natl. Acad. Sci. USA* 101, 865–870. <https://doi.org/10.1073/pnas.2630225100>.
107. Oberlander, J.G., and Woolley, C.S. (2016). 17 β -Estradiol Acutely Potentiates Glutamatergic Synaptic Transmission in the Hippocampus through Distinct Mechanisms in Males and Females. *J. Neurosci.* 36, 2677–2690. <https://doi.org/10.1523/JNEUROSCI.4437-15.2016>.
108. Gnocchi, D., and Bruscalupi, G. (2017). Circadian Rhythms and Hormonal Homeostasis: Pathophysiological Implications. *Biology* 6, 10. <https://doi.org/10.3390/biology6010010>.
109. Mogavero, F., van Zwieten, K., Buitelaar, J.K., Glennon, J.C., and Henckens, M.J.A.G. (2022). Deviant circadian rhythmicity, corticosterone variability and trait testosterone levels in aggressive mice. *Eur. J. Neurosci.* 55, 1492–1503. <https://doi.org/10.1111/ejn.15632>.
110. Colldén, H., Nilsson, M.E., Norlén, A.K., Landin, A., Windahl, S.H., Wu, J., Gustafsson, K.L., Poutanen, M., Ryberg, H., Vandenput, L., et al. (2022). Comprehensive Sex Steroid Profiling in Multiple Tissues Reveals Novel Insights in Sex Steroid Distribution in Male Mice. *Endocrinology* 163, bqac001. <https://doi.org/10.1210/endocr/bqac001>.
111. Cánovas, R., Daems, E., Campos, R., Schellinck, S., Madder, A., Martins, J.C., Sobott, F., and De Wael, K. (2022). Novel electrochemiluminescent assay for the aptamer-based detection of testosterone. *Talanta* 239, 123121. <https://doi.org/10.1016/j.talanta.2021.123121>.
112. Berens, P. (2009). CircStat: A MATLAB Toolbox for Circular Statistics. *J. Stat. Soft.* 31, 1–21. <https://doi.org/10.18637/jss.v031.i10>.
113. Holtmaat, A., and Svoboda, K. (2009). Experience-dependent structural synaptic plasticity in the mammalian brain. *Nat. Rev. Neurosci.* 10, 647–658. <https://doi.org/10.1038/nrn2699>.
114. Westwood, F.R. (2008). The female rat reproductive cycle: a practical histological guide to staging. *Toxicol. Pathol.* 36, 375–384. <https://doi.org/10.1177/0192623308315665>.
115. Kislin, M., Mugantseva, E., Molotkov, D., Kulesskaya, N., Khirug, S., Kirilkin, I., Pryazhnikov, E., Kolikova, J., Toptunov, D., Yuryev, M., et al. (2014). Flat-floored Air-lifted Platform: A New Method for Combining Behavior with Microscopy or Electrophysiology on Awake Freely Moving Rodents. *J. Vis. Exp.* 88, e51869. <https://doi.org/10.3791/51869>.
116. Pachitariu, M., Stringer, C., Schröder, S., Dipoppa, M., Rossi, L.F., Carandini, M., and Harris, K.D. (2017). Suite2p: beyond 10,000 neurons with standard two-photon microscopy. Preprint at bioRxiv, 061507. <https://doi.org/10.1101/061507>.
117. Otsu, N. (1979). A Threshold Selection Method from Gray-Level Histograms. *IEEE Trans. Syst. Man Cybern.* 9, 62–66. <https://doi.org/10.1109/TSMC.1979.4310076>.
118. Knott, G.W., Holtmaat, A., Wilbrecht, L., Welker, E., and Svoboda, K. (2006). Spine growth precedes synapse formation in the adult neocortex in vivo. *Nat. Neurosci.* 9, 1117–1124. <https://doi.org/10.1038/nn1747>.
119. Holtmaat, A.J.G.D., Trachtenberg, J.T., Wilbrecht, L., Shepherd, G.M., Zhang, X., Knott, G.W., and Svoboda, K. (2005). Transient and persistent dendritic spines in the neocortex in vivo. *Neuron* 45, 279–291. <https://doi.org/10.1016/j.neuron.2005.01.003>.
120. Friedrich, J., Zhou, P., and Paninski, L. (2017). Fast online deconvolution of calcium imaging data. *PLoS Comput. Biol.* 13, e1005423. <https://doi.org/10.1371/journal.pcbi.1005423>.
121. Argunşah, A.Ö., Erdil, E., Ghani, M.U., Ramiro-Cortés, Y., Hobbs, A.F., Karayannis, T., Çetin, M., Israely, I., and Ünay, D. (2022). An interactive time series image analysis software for dendritic spines. *Sci. Rep.* 12, 12405. <https://doi.org/10.1038/s41598-022-16137-y>.
122. Mizrahi, A., Crowley, J.C., Shtoyerman, E., and Katz, L.C. (2004). High-Resolution In Vivo Imaging of Hippocampal Dendrites and Spines. *J. Neurosci.* 24, 3147–3151. <https://doi.org/10.1523/JNEUROSCI.5218-03.2004>.
123. Schneider, C.A., Rasband, W.S., and Eliceiri, K.W. (2012). NIH Image to ImageJ: 25 years of image analysis. *Nat. Methods* 9, 671–675. <https://doi.org/10.1038/nmeth.2089>.

STAR★METHODS

KEY RESOURCES TABLE

REAGENT or RESOURCE	SOURCE	IDENTIFIER
Bacteria and virus strains		
pENN.AAV.CamKII 0.4.Cre.SV40	Plasmid was a gift to Addgene from James M. Wilson	Addgene AAV1; 105558-AAV1
Deposited data		
Raw and analyzed data	This paper; Mendeley Data	Mendeley Data: https://www.doi.org/10.17632/fwd9b5jv9h.1
Raw dendrite images and dendrite/place cell DFF	This paper; Mendeley Data	Mendeley Data: https://www.doi.org/10.17632/fwd9b5jv9h.1
Spine analysis code	GitHub	GitHub: https://doi.org/10.5281/zenodo.15200450
Dendrite analysis code	GitHub	GitHub: https://doi.org/10.5281/zenodo.15200438
Place cell analysis code	GitHub	GitHub: https://doi.org/10.5281/zenodo.15200440
Experimental models: Organisms/strains		
Mouse: Tg(Thy1-EGFP)MJrs/J	The Jackson Laboratory	RRID:IMSR_JAX:007788
Mouse: B6.Cg-Igs ^{7m162.1(tetO-GCaMP6s,CAG-tTA2)Hzc} /J	The Jackson Laboratory	RRID:IMSR_JAX:031562
Mouse: B6.Cg-Tg(Camk2a-cre)T29-1Stl/J	The Jackson Laboratory	RRID:IMSR_JAX:005359
Software and algorithms		
MATLAB 2024b	MathWorks	RRID:SCR_001622
Suite2p	Pachitariu et al. ¹¹²	RRID:SCR_016434
ImageJ	Schneider et al. ¹¹³	RRID:SCR_003070

EXPERIMENTAL MODEL AND STUDY PARTICIPANT DETAILS

A total of $n = 17$ female mice (8–28 weeks of age) were used across experiments. For dendritic morphology experiments (Figures 1 and 2), Thy1-GFP-M (Jax Stock #007788) female transgenic mice ($n = 6$, 9–17 week old females) were used for sparse expression of GFP throughout the forebrain. For dendritic imaging experiments (Figure 3), TITL2-GC6s-ICL-TTA2 (Jax Stock #031562) transgenic mice were injected with a CaMKIIα-Cre virus (Addgene #105558-AAV1) diluted 1:10,000 in CA1 ($n = 5$, 14–28 week old females). For population imaging experiments (Figures 4 and 5), CaMKIIα-Cre (Jax Stock #005359) \times TITL2-GC6s-ICL-TTA2 (Jax Stock #031562) double transgenic mice ($n = 6$, 8–12 week old females) were bred for widespread expression of GCaMP6s in excitatory neurons.

For imaging experiments, female mice were implanted with a head plate and cranial window and imaged starting 2 weeks after recovery from surgical procedures. The animals were housed on a 12 hr light/dark cycle in cages of up to five animals before the implants, and individually after the implants. All animal procedures were approved by the Institutional Animal Care and Use Committee at University of California, Santa Barbara, CA.

METHOD DETAILS

Estrous cycle staging

All mice were regularly staged by vaginal lavage starting two weeks post-surgery (once per day prior to imaging and twice per day during imaging). Samples were collected during the light phase of the cycle using 50 μ l sterile saline pipetted into the vaginal opening and aspirated several times to obtain a vaginal cytology sample. The sample was then pipetted onto a gel subbed microscope slide and allowed to dry 24 h before staining with Shorr Stain (Sigma Aldrich). Gel subbing was performed using a gelatin/CrK(SO₄)₂ solution as previously described.¹¹⁴ Dried and stained slides were imaged under a compound brightfield OMAX microscope at 10X magnification, acquired using ToupView software. Images were first examined visually to ensure a sufficient cytology sample free of debris, then processed using EstrousNet for automated estrous stage classification.³⁶ Staging was performed by an independent experimenter blind to experimental condition.

Surgical procedures

All surgeries were conducted under isoflurane anesthesia (3.5% induction, 1.5–2.5% maintenance) in sterile conditions. Meloxicam (2 mg kg⁻¹, subcutaneous) was administered preoperatively to reduce inflammation and the scalp was infiltrated with lidocaine

(5 mg kg⁻¹, subcutaneous) prior to the incision. The scalp overlying the dorsal skull was sanitized and removed. The periosteum was then removed with a scalpel and the skull was abraded with a drill burr to improve adhesion of dental acrylic.

For transverse hippocampal imaging (Figures 1, 2, and 3), we used a custom-designed glass microperiscope (Tower Optical) consisting of a 1 × 1 × 1 mm³ cubic base and a 1 mm right angle prism, with a total length of 2 mm on the longest side.³⁷ The hypotenuse of the right-angle prisms were coated with enhanced aluminum for internal reflectance. The microperiscope was attached to a 4 mm diameter coverglass (Warner Instruments) with a UV-cured optical adhesive (Norland, NOA61). Prior to implantation, the skull was soaked in sterile saline and the cortical vasculature was inspected to ensure that no major blood vessels crossed the incision site. If the cortical vasculature was suitable, a 3-4 mm craniotomy was made over the implantation site (centered at 2.0 mm posterior, 1.2 mm lateral to Bregma). For implantation, a 1 mm length anterior-to-posterior incision was made through the dura, cortex, and septal (mediodorsal) tip of the hippocampus a sterilized diamond micro knife (Fine Science Tools, #10100-30) mounted on a manipulator. The incision was centered at -2.1 mm posterior, 1.2 mm lateral (relative to Bregma) and lowered to a depth of 2.2mm. Gelfoam (VWR) soaked in sterile saline was used to remove any blood from the incision site. Once the incision site was free of bleeding, the craniotomy was submerged in cold sterile saline, and the microperiscope was lowered into the incision using a manipulator, with the imaging face of the microperiscope facing lateral. Once the microperiscope assembly was completely lowered into the CA1 such that the coverglass was flush with the skull, the edges of the window were sealed with silicon elastomer (Kwik-Sil, World Precision Instruments), then with dental acrylic (C&B-Metabond, Parkell) mixed with black ink. The dental acrylic was applied such that it did not protrude substantially over the window, to avoid scratching the objective lens surface. Given the working distance of the objective used in this study (3 mm), the microperiscope implant enabled imaging from 2250–2600 μm below the coverglass surface, corresponding to approximately 150–500 μm into the transverse hippocampus (the 150 μm of tissue nearest to the microperiscope face was not used for imaging).

For imaging CA1 soma populations (Figures 4 and 5), we used a custom-designed glass cylinder (Tower Optical) measuring 1.4 mm in diameter, with a length of 1.4 mm. The cylinder was attached to a 4 mm diameter coverglass (Warner Instruments) with a UV-cured optical adhesive (Norland, NOA61). Prior to implantation, the skull was soaked in sterile saline and the cortical vasculature was inspected to ensure that no major blood vessels crossed the implantation site. If the cortical vasculature was suitable, a 3 mm craniotomy was made over the implantation site (centered at 2.0 mm posterior, 1.8 mm lateral to Bregma). For implantation, the dura was removed from over the implant region using fine forceps (FST), and the tissue immediately over the hippocampus was removed with a 1.5 mm diameter sterile biopsy punch, which was lowered 1 mm into the tissue using a micromanipulator, centered at the implantation site and tilted 10 degrees laterally. A small amount of negative pressure was manually applied to the biopsy punch during withdrawal to remove a 1.5 mm diameter plug of cortical tissue overlying the hippocampus. Gelfoam (VWR) soaked in sterile saline was used to remove any blood from the incision site. Once the incision site was free of bleeding, the craniotomy was submerged in cold sterile saline, and the glass cylinder was lowered into the incision using a micromanipulator until the bottom surface was flush with the dorsal surface of the hippocampus. The implant was tilted 10 degrees laterally to conform to the surface of the hippocampus. Once the implant was placed, the edges of the window were sealed with silicon elastomer (Kwik-Sil, World Precision Instruments), then with dental acrylic (C&B-Metabond, Parkell) mixed with black ink. For these experiments, the imaging plane was approximately 150–200 μm below the bottom of the cylinder to allow imaging of the stratum pyramidale of subregion CA1.

After implantation of the glass microperiscope or cylinder, a custom-designed stainless steel head plate (<https://www.emachineshop.com/>) was affixed using dental acrylic (C&B-Metabond, Parkell) mixed with black ink. After surgery, mice were administered carprofen (5–10 mg kg⁻¹, oral) every 24 hr for 3 days to reduce inflammation. The microperiscope design (v1_{CA1}) and head fixation hardware designs are available on our institutional lab website (<https://goard.mcdb.ucsb.edu/resources>).

Floating chamber setup, training, and recording

For measurement of spatial responses, mice were head-fixed in a floating carbon fiber chamber (NeuroTar, Mobile HomeCage).¹¹⁵ The chamber base was embedded with magnets to allow continuous tracking of the position and angular displacement of the chamber relative to the mouse. Behavioral data were collected via the Mobile HomeCage motion tracking software (NeuroTar, versions 2.2.014, 2.2.1.0, and 3.1.5.2). During imaging experiments, image acquisition was triggered using a TTL pulse from the behavioral software to synchronize the timestamps from the 2P imaging and chamber tracking.

A carbon fiber arena (250 mm diameter) with an excluded inner circle (140 mm) was used to create a circular track with a circumference of 61.26 cm (measured along the center of the track). Visual cues on both the outer and inner walls were made with photoluminescent tape (Lockport), and the experiments were conducted in near-darkness, reducing the influence of distal cues outside of the chamber.⁶⁵ Tracks were designed with two sets of cues (A, B) to stimulate place cell activity, with one cue used in both sets at the beginning of the track (star) to enable tests of remapping between environments. Cues were charged for 30 minutes under UV light then allowed to rest for 30 minutes to reach a steady phosphorescent intensity before beginning recordings. The first set of cues were paired with a foam floor insert and the second set of cues were paired with a perforated bubble wrap insert to provide distinct tactile cues. During home cage rest intervals between imaging sessions, the experimenter scrubbed the chamber with a veterinary-grade disinfectant and deodorizer (Rescue), to eliminate the influence of odor cues between environments.

After water restriction to 85% of initial bodyweight, mice were acclimated to the arena by the following steps (Figure S5E): (1) On the first day the mice were placed into the chamber with cues for environment A and allowed to freely explore without head fixation for 10 min. Small pieces of hydrogel were scattered along the track to encourage exploration. A piece of plexiglass with drilled air holes

was placed on top of the arena to keep the mice from climbing out. They were then returned to their home cage for 5 minutes while environment B was prepared, then these steps were repeated for environment B. This was repeated for 3 days with exposures to each environment increasing by 5 minutes on each consecutive day. (2) On the fourth day, the mice were head-fixed to a crossbar extending over the floating chamber (Figure 4C) and allowed to freely explore the floating chamber for 5 min with water reward given at the completion of each lap. Air flow (2–5.5 psi) was adjusted to maximize steady walking/running. The mice were then placed back in their home cage before being re-head fixed in environment B and allowed to explore for another 5 minutes. For the next 3 days the head fixation time was increased by increments of 2 min in each environment, as long as the mice showed increased distance walked and percent time moving. (3) On day 8, the mice began the complete head fixation sequence of three environments (A > B > A'), where they were allowed to explore each environment for 5 minutes with a 5-minute rest period in the home cage between each exposure. The exposure period increased by 5 minutes every four days until the mice were comfortably running for 15 minutes in each environment on day 19. (6) On the last two days of the training period (days 20 and 21), mice were acclimated to the full trial setup, in which they were first allowed to freely explore each environment for 20 minutes before being head-fixed and placed on the 2P microscope to allow habituation to the microscope noise, and for each environment were only allowed to run 10 laps under a speed threshold of 200 mm/s (laps over the speed threshold were not counted towards the total number of laps run). This was to account for overexertion during exposure to the first environment, and prevent tiring by the third environment. (5) On day 22, after mice were fully habituated, recording sessions on the 2P microscope were performed every 12 hours for 4.5–11 days to ensure that at least one imaging sessions was taken during each stage of the estrous cycle.

Behavior data was acquired using Mobile HomeCage motion tracking software (NeuroTar) and analyzed using custom software. Since the Mobile HomeCage motion tracking software sampling rate was faster than the 2P imaging frame rate, all behavioral variables (speed, location, polar coordinates, and heading) that were captured within the acquisition of a single 2P frame were grouped together and their median value was used in future analysis. For the polar angle (used to determine the location bin of the mouse along the 1D track), the median was computed using an open-source circular statistics toolbox (CircStat 2012a) written for MATLAB.¹¹² We removed any time points when the mouse was not moving, as is standard for measurement of place fields.³⁹ To do this, we smoothed the measured instantaneous speed and kept time periods > 1 s that had speeds greater than 20 mm/s (adding an additional 0.5 s buffer on either side of each time period).

Two-photon imaging

After recovery from surgery and behavioral acclimation, GFP or GCaMP6s fluorescence was imaged using an Investigator 2P microscopy system with a resonant galvo scanning module (Bruker). For fluorescence excitation, we used a Ti:Sapphire laser (Mai-Tai eHP, Newport) with dispersion compensation (Deep See, Newport) tuned to $\lambda=920$ nm. Laser power ranged from 40 to 80 mW at the sample depending on GCaMP6s expression levels. Photobleaching was minimal (<1% min⁻¹) for all laser powers used. For collection, we used GaAsP photomultiplier tubes (H10770PA-40, Hamamatsu). A custom stainless-steel light blocker (eMachine-shop) was mounted to the head plate and interlocked with a tube around the objective to prevent light from the environment from reaching the photomultiplier tubes. For imaging, we used a 16 \times /0.8 NA microscope objective (Nikon) to collect 760 \times 760 pixel frames with field sizes ranging from 829 \times 829 μm (1x zoom) to 51.8 \times 51.8 μm (16x zoom). Images were collected at 20 Hz and stored at 10 Hz, averaging two scans for each image to reduce shot noise.

For longitudinal imaging of dendritic structure and activity, imaging fields on a given recording session were aligned based on the average projection from a reference session, guided by stable structural landmarks such as specific neurons and dendrites. Physical controls were used to ensure precise placement of the head plate, and data acquisition settings were kept consistent across sessions. Images were collected every 12 hours for 8–11 days in structural imaging experiments, and 4.5–5 days in calcium imaging experiments, with length of session dependent on the periodicity of the estrous cycles prior to imaging, which here ranged from 4 to 5.5 days. Imaging sessions were performed at approximately 6am and 6pm every day for consistency.

Two-photon image post-processing

Images were acquired using PrairieView acquisition software (Bruker) and converted into multi-page TIF files for analysis with MATLAB (Mathworks).

For spine imaging, registration and averaging was performed for each z-plane spanning the axial width of the dendrite to ensure all visible spines were captured. A gaussian distribution was fit to the intensity of the dendrite, and the images were weighted according to the fit. Dendritic segments then underwent rigid global registration across days. Dendrite registration was performed using the MATLAB imregister function with regular-step gradient descent optimization and a mean square error metric configuration. The registered images underwent high-pass filtering to extract low contrast spine features using code adapted from Suite2P's enhanced mean image function.¹¹⁶ The resulting ROIs were binarized using Otsu's global threshold method for spine classification.¹¹⁷ In most cases, the global threshold successfully isolated a single prominent dendrite. In fields with higher background containing undesired dendrites, extraneous dendrites were manually masked. To identify spines that fell below the global threshold, the user manually specified incrementally lower thresholds from which to select spines that were excluded in the initial binarization. Spines above the global threshold with an area of $>1 \mu\text{m}^2$ were included in our analysis. To classify each spine as one of the four major morphological classes, we performed the following steps: First, we found the base of the spine by identifying the region closest to the dendritic shaft. Second, we calculated the length of the spine by taking the Euclidean distance between the midpoint of the spine base

and the most distant pixel. Third, three vectors evenly spaced between the base and top of the spine were drawn perpendicular to the main axis, the first and third of which were identified as the head and neck, respectively. The logical spine mask was superimposed onto the normalized gaussian averaged image, and integrated brightness was calculated as the sum of the pixels in the masked area.^{118,119} Finally, spines were classified in the four categories, considering the following threshold parameters: mean width, head/neck width ratio, length/mean width ratio, and integrated brightness (Figure S2A).

For calcium imaging sessions, the TIF files were processed using the Python implementation of Suite2P.¹¹⁶ We briefly summarize their pipeline here. First, TIFs in the image stack undergo rigid registration using regularized phase correlations. Next, regions of interest (ROIs) are extracted by clustering correlated pixels, where a low-dimensional decomposition is used to reduce the size of the data. The number of ROIs is set automatically from a threshold set on the pixel correlations. We manually checked assigned ROIs based on location, morphology, and $\Delta F/F$ traces.

Since the hippocampal pyramidal cells are densely packed, we perform local neuropil subtraction using custom code (GitHub: <https://github.com/ucsb-goard-lab/two-photon-calcium-post-processing>) to avoid neuropil contamination. The corrected fluorescence was estimated according to:

$$F_{\text{corrected}}(n) = F_{\text{soma}}(n) - \alpha(F_{\text{neuropil}}(n) - \bar{F}_{\text{neuropil}}),$$

where F_{neuropil} was defined as the fluorescence in the region $<30\mu\text{m}$ from the ROI border (excluding other ROIs) for frame n . $\bar{F}_{\text{neuropil}}$ was F_{neuropil} averaged over all frames. α was chosen from [0, 1] to minimize the Pearson's correlation coefficient between $\bar{F}_{\text{neuropil}}$ and F_{neuropil} . The $\Delta F/F$ for each neuron was then calculated as:

$$\frac{\Delta F}{F} = \frac{F_n - F_0}{F_0},$$

where F_n is the corrected fluorescence ($F_{\text{corrected}}$) for frame n and F_0 is defined as the first mode of the corrected fluorescence density distribution across the entire time series.

We deconvolved this neuropil subtracted $\Delta F/F$ to obtain an estimate for the instantaneous spike rate, which we used for the computation of neurons' spatial information and mean event rate (Figures S6C and S6D), as well as conditional probability of spike occurrence in dendritic compartments (Figures S4A and S4B). This inferred spike rate was obtained via a MATLAB implementation of a sparse, nonnegative deconvolution algorithm (OASIS) used for Ca^{2+} recordings.¹²⁰ We used an auto-regressive model of order 2 for the convolution kernel.

Spine imaging data analysis

After rigid registration, high-pass filtering, and binarization of the dendritic segment, individual spines were extracted based on standard morphological criteria.¹¹³ Spines projecting laterally from the dendritic segment were extracted and analyzed as individual objects, as described previously. The sum of the members of each spine class, as well as the total number of all spines, was recorded for each session. Spine totals (S_{total}) were then broken down into 10 μm sections of the dendritic segment (S_{section}) using the following calculation

$$S_{\text{section}}(n) = \frac{S_{\text{total}}(n)}{\left(D_{\text{length}} \times \frac{F_{\mu\text{m}}}{F_{\text{pixels}}}\right)} \times 10,$$

where length of the dendritic segment, D_{length} , was determined by skeletonizing the dendritic shaft to 1 pixel in diameter, then taking the area of the pixels. F_{pixels} is the FOV in pixels, which here was 760 pixels in each axis at 16 \times magnification, and $F_{\mu\text{m}}$ is the FOV in μm , which was 52 μm in each axis.

Turnover was estimated at 12 hr increments; turnover here is defined as the net change in spines per session for each morphological class. Percent addition/subtraction, T , was calculated as

$$T = \frac{N_t}{N(t)} \times 100,$$

where N_t is spines that have been added or subtracted and $N(t)$ is the total average number of spines. To determine the total population of spines on each dendrite, dendritic segments first underwent global registration across days, as described previously. After registration the centers of all spines across all days were overlaid, and spines falling under a spacing threshold of 1.7 μm were considered to be the same spine. The remaining ROIs represented the total cumulative population of dendritic spines across the time series.

Global registration was rigid so that spine shape would not be warped and misclassified as a different spine type, however small differences in dendritic morphology made the visualization of the exact same spine location difficult across days. Because of this, we also employed local registration, in which an 80 \times 80 pixel ROI around the centroid of the dendritic spine was cut out and independently registered against the time series of images using the same registration parameters as in global registration. This is consistent with previous dendritic spine registration techniques.¹²¹ These images were further broken down by spine type and registered to each other, then averaged, resulting in an average projection of each classification (Figure S2B). Randomly selected examples of each spine type are also displayed to illustrate face validity of the classification procedure (Figures S2F–S2I).

The coordinates of the locally registered spine ROI from the gaussian averaged image were applied to the same region on the binarized image, and a 40 x 40 pixel series of both average projection and binarized ROI images were displayed in a GUI format, along with recording number, so that the experimenter could manually confirm that the same spine was detected across days, and that the classification of the spine as either present or not present was correct (Figure S1). Manual curation of spines was performed blind to estrous stage.

Once spine numbers across recordings were confirmed and normalized to spines per 10 μm , recordings were interpolated to an archetypal cycle, where each stage was repeated twice and the cycle was repeated three times (i.e. D-D-P-P-E-E-M-M x3; Figures 1F, S3A, and S3B). Stages were first interpolated to a standard two-recording length, such that stages that lasted just one recording were repeated twice, and stages that lasted more than 2 recordings were averaged so that the first timepoint was the average of the first half of recordings within that stage (rounded up for stages with odd number recordings), and the second timepoint was the average of the second half. Stages lasting two recordings were left as-is. The resulting vector was input into the archetypal cycle such that the first observed stage determined the starting location of the vector. For instance, a recording beginning with proestrus would begin at the third slot in the archetypal cycle. This method was employed instead of circularizing the cycle to preserve the time course of turnover within dendrites.

To calculate the survival fraction curve $S(t)$, we determined which spines were present at time t_n that were not present at time t_0 .^{21,49,122} For all spines this was considered any spine that was present on recording session 1 regardless of estrous stage. For proestrus-added spines, only spines for which the diestrus stage before proestrus as well as an entire cycle after proestrus were recorded were included in the analysis. Spines were considered to be proestrus-added when no spine was present in diestrus, regardless of when during the proestrus stage they appeared. The survival fraction of these spines was quantified such that recording 1 was the recording at which the spine appeared, and recording 2 was the first recording of the estrus stage immediately following proestrus. Survival fraction was quantified as

$$S(t) = \frac{N_r(t_n)}{N(t_0)} \times 100,$$

where $N_r(t_n)$ are the total spines at t_n that were also found in t_0 , and $N(t_0)$ are the total number of spines that were present in t_0 .

To calculate transition matrices (Figure 2F), the population of spines present in diestrus, proestrus, and estrus were first classified, as well as the classifications of those spines in the stage immediately following (i.e. diestrus > proestrus, and proestrus > estrus). The transition matrices were calculated as the probability that a spine of a particular classification (e.g., mushroom) would transition to each of the other classifications (mushroom, stubby, thin, filopodia, no spine) during the stage transition. Matrices were pseudocolored to indicate transitions to more stable spine classes (red, above unity line), less stable spine classes (blue, below unit line) or no change (greyscale).

For PCA analysis (Figure S2D), vectors measuring morphological parameters (mean width, head/neck width ratio, length/mean width ratio, and integrated brightness) were used to create a 4-dimensional feature space. The first two principal components were plotted against each other for visualization.

For analysis of distance-dependent spine turnover, the distribution of spines along the dendritic arbor was calculated and the 33rd and 67th percentiles were used to determine cutoffs for proximal, medial, and distal groups (Figure S3C). Spine turnover and percent change in density were calculated for each dendrite within distance groups, as described above (Figures S3D and S3E).

Dendritic calcium imaging data analysis

For dendritic calcium imaging, mice were allowed to run head-fixed around the floating chamber for 15 minutes, during which they completed at least 10 but up to 20 laps. Visual and textural cues in the chamber were the same used for environment A in remapping analysis. To analyze dendritic imaging data, the user first extracted ROIs using a custom GUI interface which overlaid the average projection on top of a pixel-wise activity map calculated using a modified kurtosis measure and asked the user to manually draw ROIs around the cell of interest, which was highlighted in a separate window to guide ROI selection. The soma was selected using an elliptical ROI, and dendrite was selected using a freehand object. The somatic ROI was maintained for the rest of the analysis, but the dendritic ROI was automatically redrawn by dilating the skeletonized image defined by the outer bounds of the hand-drawn ROI with a structuring element 10-pixels in diameter. This helped to eliminate user error and standardize dendritic ROI selection. The sub-ROIs were created by splitting up the previously defined dendritic ROI into serial sections with a specified length, here 6 μm . A subset of somatic ROIs and their respective dendritic and sub-ROIs were identified as place cells (see Population calcium imaging data analysis, below), and put through the same steps to determine estrous-dependent properties (Figures S4C–S4G).

Next, $\Delta F/F$ was calculated as is previously described for soma ROIs, dendrite ROIs, and subROIs. Neuropil was not subtracted in order to avoid inadvertently removing relevant signal, but is expected to be low due to sparse expression and the localization of the ROI around the dendrite.

Coupling between the soma and dendrites or the soma and subROIs were calculated using a Pearson's correlation between $\Delta F/F$ traces extracted from the respective ROIs (Figures 3G and 3J). As an alternate measure, inferred spikes were calculated for each soma and dendrite as described previously, and were used to calculate the conditional probability of observing a dendritic event given a somatic event (Figures S4A and S4B).⁶⁴ Conditional probability of observing a dendritic event given a somatic event was quantified as

$$P_{(d \mid s)} = \frac{\sum_{i=1}^{N_s} 1(\min|t_{D_i} - t_{S_i}|) \leq b}{N_s},$$

where N_s is the total number of discrete somatic events, t_{D_i} is the start of the event i in the dendrite, t_{S_i} is the start of the event i in the soma, and b is the buffer time, here defined as one frame.

To identify bAPs, somatic events were identified in the somatic $\Delta F/F$ trace by extracting significantly elevated sections of the calcium trace, defined as three standard deviations above the mean, and aligned with dendritic $\Delta F/F$.^{51,63} Occasionally short sections of an AP fell below threshold, so gaps of < 5 frames (0.5 s) were interpolated to avoid counting single bAPs multiple times. During the AP event, subROI responses along the length of the dendrite were isolated and averaged, then normalized to the average somatic $\Delta F/F$ during the bAP interval. Each bAP was fit with an exponential decay function to determine the decay constant and goodness of fit. The exponential decay function was calculated as

$$F(x) = F_{soma} \times e^{-\lambda x},$$

where F_{soma} is the $\Delta F/F$ at the soma (normalized to 1), x is the distance in microns, and λ is the decay constant.

The cumulative population of bAPs had an averaged r^2 of 0.81 ± 0.06 (mean \pm sem), and a threshold r^2 value of 0.7 was set to only consider good-quality bAP exponential fits. The length constant (λ), was calculated as the decay constant of the fit exponential decay function, and is equivalent to the distance a bAP travels before decaying to 37% of its initial amplitude. Length constants were capped at 400 μm , the maximum length of any dendrite in the dataset. The resulting bAP length constants were averaged across events within cells, and analyzed as a function of estrous stage (Figure 3M).

Population calcium imaging data analysis

For somatic calcium imaging experiments during exploration of the air-floated chamber, processed and synchronized behavioral data and 2P imaging data were used to identify place cells as follows.

First, the 1D track was divided into 72 equal bins (each ~ 0.85 cm in length). Activity as a function of position (spatial tuning curves) was computed for each lap, with activity divided by the occupancy for each binned location. We observed that in certain cases, the mice traversed the track at high speeds. To avoid misattribution of slow calcium signals to spatial bins, any lap where the average instantaneous speed was greater than 200 mm/s was removed and not considered for further analysis (an average of 6% of laps were removed). To assess the consistency of spatial coding of each cell, we randomly split the laps into two groups and computed the correlation coefficient between the averaged spatial tuning curves. We then did the same for shuffled data in which each lap's spatial tuning curve was circularly permuted by a random number of bins. Note that this was done for each lap, to avoid trivial effects that might emerge from circularly permuting data that was stereotyped along the track. This was performed 500 times, and the distribution of actual correlation coefficient values was compared to the distribution of circularly shuffled values using a two-sample Kolmogorov-Smirnov test ($\alpha = 0.01$). The average correlation coefficient for actual data for each place cell was used as a metric to determine lap-wise stability across estrous stages (Figure S6E). The distribution of these values had to pass a Cohen's D analysis, having a score of greater than 1.2. A cell that passed both of these tests was considered a 'consistent' cell.³⁷

To identify a neuron as a place cell, the neuron had to pass the consistency test, in addition to being fit well by a Gaussian function, $R_{\Delta F/F} = A_0 + A e^{\left(\frac{(X-B)}{C}\right)^2}$, with $FWHM = 2C\sqrt{\ln 2}$. Note that in this convention, $C^2 = 2\sigma^2$. Specifically, we required that: (1) the adjusted $R^2 > 0.375$; (2) $2.5 \text{ cm} < FWHM < 30.6 \text{ cm}$ (50% of track length); (3) $A > 0$; (4) $\frac{A}{A_0} > 0.50$. Cells that met these conditions were characterized as place cells; with place fields at the location of maximal activity and width defined as the FWHM. Note that these criteria are somewhat strict compared to traditional place field criteria. When tested with data in which individual laps were time shuffled, the approach yielded a false positive rate of 0%. In remapping experiments, only place cells that passed these qualifications in environment A were considered for further analyses.

To compute the spatial information of cell j (SI_j), we used the following formula,

$$SI_j = \frac{1}{\bar{a}_j} \sum_{k=1}^{72} p(k)a_j(k)\log_2 \left[\frac{a_j(k)}{\bar{a}_j} \right],$$

where a_j is the mean inferred spike rate of cell j , $a_j(k)$ is the mean inferred spike rate of cell j at position bin k , and $p(k)$ is the probability of being at position bin k . We divide by a_j to have SI_j in units of bits/inferred spike (Figure S6C).

For further analysis, calcium traces extracted from GcaMP6s recordings were corrected for slow changes in fluorescence, as previously described.⁶⁹ Briefly, calcium transients were calculated by sequentially subtracting the eighth percentile of the fluorescence distribution, calculating baseline fluorescence using all points that did not exceed 3 standard deviations of the total signal, and using the resulting $\Delta F/F$ trace to calculate parameters for transient detection that yielded a false positive rate of <5%.⁶⁹ All baseline fluorescence then was masked to zero.⁶⁹

For single cell analysis, differences between peaks in the same place cell across three environments was measured in bins, then converted to circular distance in cm (Figure 5C). For population vector analysis, population vectors were defined for each 0.85-cm bin

of the lap-averaged tuning curves (72 bins in total) from all cells in the experimental group for each of the three environments. Pearson's correlations were calculated between vectors of the same spatial bin across the three environments ($A > B > A'$) and averaged for every occurrence of the four stages within each animal. Because recordings in different stages had different numbers of cells, for recordings within each animal PVec correlations were bootstrapped across 100 iterations and $n = 6$ mice, sampling the minimum number of cells from each stage with replacement (Figure 5D).

To further test estrous-dependent changes in spatial coding, we used a linear model to predict position in circular environments (B, A') based on modeled firing rate distributions from a reference environment (A). For each iteration, cells were randomly sampled with replacement, using the minimum number of cells across stages for each animal ($n = 577$ neurons across 6 animals). We sampled 7 trials, the minimum number of trials across all recordings, from each environment for each cell. From the responses to environment A, the firing rate distribution was determined for each neuron. For each position in environments B and A', the response of each neuron was multiplied by the Environment A firing rate distribution, and the scaled firing rate distribution were summed across all neurons and normalized to generate an estimated probability for each position. We then plotted the probability density of the estimated position at each actual position in environments B and A', averaged over 100 iterations to account for sampling variability (Figures 5E and S7).

Histology

Mice were euthanized with CO₂ and transcardially perfused using 4% paraformaldehyde in 1X phosphate-buffered solution (PBS). Extracted brain tissue was immersion fixed overnight in the same solution at 4°C. After 24 hr, samples were moved to 1X PBS. Subsequently, 100 µm coronal sections were cut using a vibratome (Leica). Sections were then mounted on gel subbed slides using Vectashield Antifade Mounting Medium with DAPI (Vector laboratories Inc; H-1200-10) and sealed under #0 coverslips. Images were taken using a Leica SP8 resonant scanning confocal at 64X magnification and grid stitched in ImageJ.¹²³

QUANTIFICATION AND STATISTICAL ANALYSIS

Spine turnover was evaluated in each time point using a linear mixed effect model against a grand mean with random effects for mouse (Figure 1F; Table S1A). In experiments evaluating turnover as a function of spine type, linear mixed effect models were generated for each spine type, with fixed effects for stage and random effects for mouse (Figure 1G; Table S1A). For dendritic activity comparisons, as well as comparisons between single place cell responses, linear mixed effect models were used with fixed effects for stage and random effects for mouse. Pairwise linear mixed effect models were used to evaluate contrasts between specific stages ($n = 6$ comparisons, Bonferroni corrected; Figures 3G, 3J, 3M, 5C, S3D, S3E, S4B, S4E–S4G, and S6B–S6H; Tables S1B–S1F). Post-hoc Tukey's HSD was used to evaluate the percentage of place cells across stages in each mouse ($n = 6$ comparisons, Bonferroni corrected; Figure S6A; Table S1E). Very small p-values ($<10^{-4}$) were capped at $p \leq 10^{-4}$ as a lower bound on reasonable probabilities. In population comparisons where bootstrapping was employed, 95% confidence intervals were used to evaluate significance (Figures 5D and S7D). When performing bootstrapping, data were randomly sampled with replacement.